

THE PROPERTIES OF X-RAY-SELECTED ACTIVE GALACTIC NUCLEI. I. LUMINOSITY FUNCTION, COSMOLOGICAL EVOLUTION, AND CONTRIBUTION TO THE DIFFUSE X-RAY BACKGROUND¹TOMMASO MACCACCARO,^{2,3} ROBERTO DELLA CECA,⁴ ISABELLA M. GIOIA,^{3,5} SIMON L. MORRIS,⁶ JOHN T. STOCKE,⁷ AND ANNA WOLTER^{3,8}*Received 1990 July 23; accepted 1990 November 14*

ABSTRACT

The X-ray luminosity functions (XLF) of X-ray-selected active galactic nuclei (AGNs) and its cosmological evolution are derived and discussed. The sample utilized consists of more than 420 X-ray-selected AGNs extracted from the *Einstein Observatory* Extended Medium-Sensitivity Survey. The local ($z < 0.1$) observed XLF as well as the XLF in different redshift shells up to $z \sim 2$ have been derived. The local XLF shows a substantial flattening for $L_x \leq 5 \times 10^{42}$ ergs s⁻¹, while at higher luminosities it can be approximated by a power law. The AGN XLF obtained in a model-independent way at different redshifts gives *direct* evidence for cosmological evolution (weak for $z \leq 0.4$ and more pronounced for higher z). The data have been analyzed within the framework of pure luminosity evolution models, and the two most common evolutionary forms $L_x(z) = L_x(0)e^{Cz}$ and $L_x(z) = L_x(0)(1+z)^C$ have been considered. Best-fit values of 4.18 and 2.56, respectively, have been found for the evolution parameter C . The de-evolved X-ray luminosity function has been derived. A good fit with a broken power law (with slope $\gamma_1 = 1.35$ for $L_x(0) \lesssim 2.5 \times 10^{43}$ ergs s⁻¹ and slope $\gamma_2 = 3.05$ for $L_x(0) \gtrsim 2.5 \times 10^{43}$ ergs s⁻¹) has been obtained. There is no evidence for a further slope change outside the range of luminosities sampled (10^{42} – 10^{47} ergs s⁻¹). The simultaneous determination of the cosmological evolution and of the XLF is then used to estimate the contribution of the AGNs to the extragalactic diffuse X-ray background. Using the best-fit values for the evolution of AGNs and for their volume density, it is found that they contribute $\sim 40\%$ of the 2 keV diffuse X-ray background. About 85% of this contribution comes from objects with $L_x(0)$ between 10^{42} and 10^{44} ergs s⁻¹.

Subject headings: galaxies: nuclei — galaxies: X-rays — luminosity function — X-rays: sources

1. INTRODUCTION

The completion of the *Einstein Observatory* Extended Medium-Sensitivity Survey (EMSS; Gioia et al. 1990) and the very high identification rate presently available (96%) allow us to extract subsamples of sources suitable for statistical studies. In this paper we concentrate on the sample of X-ray-selected active galactic nuclei (AGNs)⁹ as a whole to study their X-ray luminosity function, cosmological evolution, and contribution to the X-ray background. These studies require only the X-ray flux and redshift information which is already available for 427 AGNs (Stocke et al. 1991). The analysis of different subsamples

of AGNs, of luminosity correlations, of the optical and radio luminosity function, and of the comparison of the overall properties of X-ray-selected, optically selected, and radio-selected AGNs will be published in forthcoming papers. We are aware that the sample used here is not fully identified and that a number of AGNs will be discovered among the remaining 31 unidentified sources. However, our analysis shows that the results presented here will not be changed significantly once the identification process has been completed. We have specifically addressed this point, using the available information to estimate the number of AGNs hidden among the 31 unidentified sources as well as their probable redshifts. For a full description of the EMSS, selection criterion, and data analysis, the reader is referred to the paper by Gioia et al. (1990), where the sample of sources is given, together with the classification of the optical counterpart of the identified sources.

Here we recall that the EMSS is a statistically complete and well-defined sample of 835 serendipitous X-ray sources detected in IPC images of the high Galactic latitude sky obtained with the IPC on board the *Einstein Observatory*. The EMSS has limiting sensitivities from 5×10^{-14} to 3×10^{-12} ergs cm⁻² s⁻¹ in the 0.3–3.5 keV energy band. A detailed discussion of the identification process and of the optical properties of the EMSS X-ray sources is given in Stocke et al. (1991), while the optical images of the area surrounding the EMSS sources are shown in Maccacaro et al. (1991).

The optical identification program is still in progress, and at the time of this writing (1990 September) 804 sources out of 835 have been identified (43 more than quoted in Gioia et al. 1990).

¹ This paper uses data obtained at the Multiple Mirror Telescope Observatory (MMTO), which is operated jointly by the University of Arizona and the Smithsonian Institution.

² Osservatorio Astronomico di Bologna, via Zamboni 33, 40126 Bologna, Italy.

³ Harvard-Smithsonian Center for Astrophysics, 60 Garden Street, Cambridge, MA 02138.

⁴ Dipartimento di Astronomia, Università di Bologna, via Zamboni 33, 40126 Bologna, Italy.

⁵ Istituto di Radioastronomia del CNR, via Irnerio 46, 40126 Bologna, Italy.

⁶ The Observatories of the Carnegie Institution of Washington, 813 Santa Barbara Street, Pasadena, CA 91101.

⁷ Center for Astrophysics and Space Administration, University of Colorado, Campus Box 391, Boulder, CO 80309.

⁸ Osservatorio Astronomico di Brera, via Brera 28, 20100 Milano, Italy.

⁹ As we have done in previous papers, with the term AGN we refer to both quasars and Seyfert galaxies (but not to BL Lacertae objects), i.e., to those objects showing broad and/or narrow emission lines, evidence of a nonstellar continuum, and a measurable redshift, regardless of their appearance on the Palomar Observatory Sky Survey.

Moreover, as a consequence of further spectroscopic work, a few identifications have been revised (see Stocke et al. 1991). AGNs are by far the most numerous class of objects found in a high Galactic latitude survey conducted in the soft X-ray band (0.3–3.5 keV). Of the 804 EMSS sources identified so far, 427 are AGNs. They represent $\sim 73\%$ of the entire extragalactic population.

This paper is organized as follows. In § 2 we describe our data set, and we discuss the slight incompleteness of the sample and how to take it into account in the statistical analysis. In § 3 we derive the local X-ray luminosity function as well as the luminosity function in different redshift shells. In § 4 we discuss the cosmological evolution of AGNs. In § 5 the derived luminosity function and its cosmological evolution are used to determine the AGN's contribution to the diffuse X-ray background. Finally, in § 6, a summary and conclusions are presented.

Throughout the paper a Hubble constant of $50 \text{ km s}^{-1} \text{ Mpc}^{-1}$ and a Friedmann universe with a deceleration $q_0 = 0$ are assumed.

2. THE EMSS AGN SAMPLE

The relevant data for the sample of 427 spectroscopically identified X-ray-selected AGNs used in this paper are presented in Table 1. These sources are those listed in Table 7 of Stocke et al. (1991) and identified with an AGN or, in the case of an ambiguous identification, those for which an AGN is the primary identification. Columns are as follows: (1) EMSS source name, (2) signal-to-noise ratio, (3) 0.3–3.5 keV X-ray flux in units of $10^{-13} \text{ ergs cm}^{-2} \text{ s}^{-1}$, (4) redshift, (5) logarithm of the observed monochromatic X-ray luminosity (at 2 keV, in $\text{ergs s}^{-1} \text{ Hz}^{-1}$), (6) logarithm of the observed broad-band X-ray luminosity (0.3–3.5 keV, in ergs s^{-1}).

EMSS source name, signal-to-noise ratio, and X-ray fluxes are taken from Gioia et al. (1990). Fluxes are computed assuming a power-law spectrum with energy index $\alpha = 1.0$ (derived in the spectral analysis of the extragalactic EMSS sources of Maccacaro et al. 1988) and using the measured hydrogen column density along the line of sight to each source (as reported in Stark et al. 1989; Heiles & Cleary 1979; Cleary, Heiles, & Haslam 1979). The quoted fluxes and luminosities have been corrected for absorption. (See Gioia et al. 1990 for details.) Redshifts are taken from Stocke et al. (1991).

As a consequence of the spectroscopic work carried out since the publication of Gioia et al. (1990), several new sources have been identified and a few identifications have been revised. A detailed description of the identification criteria and of the reasons behind the revision of a few identifications is given in Stocke et al. (1991), together with the discussion of a number of sources for which either the identification or the classification of the optical counterpart is ambiguous. Thus the sample of AGNs used here is slightly different from that of Gioia et al. (1990). Thirty-four of the sources listed in Table 1 were in fact unidentified in Gioia et al. (1990) and listed as class 1 (31) or class 2 (3); two were classified as stars and one as a cluster. These 37 sources are indicated (see the footnotes to Table 1). Furthermore, five sources (MS 1019.0+5139, MS 1157.3+5548, MS 1208.2+3945, MS 1309.1+3208, and MS 1332.6–2935) which were classified as AGNs in Gioia et al. (1990) are now classified differently (see Stocke et al. 1991).

Even though the identification rate is very high (96%) and, as a consequence, most of the results are not significantly affected by the resulting incompleteness, we have attempted to

reduce the effect of this incompleteness further as described below. We have used the information on the composition of the EMSS sample as a function of flux (see Table 2) to estimate the fraction of AGNs expected among the unidentified sources. At the flux level characteristic of the unidentified sources, AGNs constitute $\sim 80\%$ of the extragalactic population. Taking into account that four of the 31 unidentified sources are classified as of probable Galactic origin (class 2), we expect that ~ 21 AGNs will be added to those of Table 1 upon completion of the work of identification. We have thus extracted, using a random process, 21 “expected” AGNs from the 27 unidentified sources of probable extragalactic origin. These objects are listed in Table 3, which is organized in a manner similar to that of Table 1. As can be seen from Table 3, redshifts have been assigned to the “expected” AGNs. The procedure followed is based on the relationship between redshift and X-ray flux observed in the 427 spectroscopically classified AGNs for which the redshift has been measured (see Fig. 1). As expected, the AGN mean redshift increases with decreasing flux; the dispersion around the mean, however, is significant and prevents assignment of a redshift value to the various objects simply on the basis of their flux. Therefore, to take into account this large dispersion, we have constructed the AGN redshift probability distribution for different flux groups. We have then used a random number generator to assign a redshift to each “expected” AGN, using its flux to choose the appropriate redshift probability distribution.

These 21 objects combined with the 427 spectroscopically identified AGNs constitute the sample used throughout the present paper. As we show in § 4.2, this procedure does not introduce significant uncertainties in the analysis of the cosmological evolution.

The redshift and X-ray luminosity distributions for the AGN sample are shown in Figures 2 and 3, respectively. The shaded area indicates the distribution of the “expected” AGNs.

The mean redshift is 0.42, and 50% of the objects have redshift less than 0.27. X-ray luminosities are distributed over five orders of magnitude, from $\sim 10^{42}$ to $\sim 10^{47}$, the mean logarithmic broad-band luminosity being 44.25, and the luminosities of

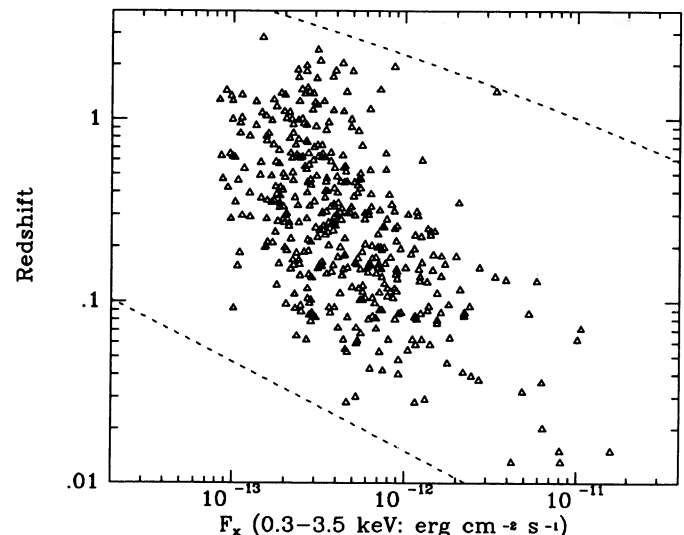


FIG. 1.—The 427 spectroscopically classified AGNs plotted in the $\log F_x$ - $\log z$ plane. The two dotted lines represent the locus with L_x equal to 10^{42} and $10^{47} \text{ ergs s}^{-1}$.

TABLE 1
 RELEVANT DATA FOR THE SAMPLE OF 427 SPECTROSCOPICALLY IDENTIFIED X-RAY-SELECTED AGNS

Source Name	S/N	Flux 0.3-3.5 keV	z	logLx 2 0.3-3.5 keV	logLx 2 0.3-3.5 keV	Source Name	S/N	Flux 0.3-3.5 keV	z	logLx 2 0.3-3.5 keV	logLx 2 0.3-3.5 keV
(1)	(2)	(3)	(4)	(5)	(6)	(1)	(2)	(3)	(4)	(5)	(6)
MS0002.4+1604	6.0	4.54	0.514	26.91	44.91	MS0129.1-2237	5.5	5.70	0.113	25.49	43.54
MS0002.5-4205	4.5	6.11	0.154	25.82	43.86	MS0130.0+0330	4.4	3.29	0.716	27.11	45.13
MS0007.1-0231	9.1	9.56	0.087	25.52	43.53	MS0131.1+0342	6.0	7.42	0.255	26.40	44.42
MS0007.8-3543	5.0	3.64	0.093	25.12	43.17	MS0132.5-4151	5.5	6.52	0.172	25.95	43.99
MS0012.5-0024	4.8	2.41	1.695	27.99	46.01	MS0135.0+0339	5.3	2.35	0.637	26.83	44.85
MS0017.3+1540	9.5	6.54	0.083	25.32	43.32	MS0135.3+0324	4.9	1.69	0.98:	27.17	45.19
MS0020.4+0058	4.6	2.32	0.720	26.96	44.98	MS0135.4+0256	6.8	4.41	0.150	25.67	43.69
MS0036.5+2103	4.2	2.44	1.250	27.62	45.64	MS0136.0-5614	11.2	22.22	0.086	25.87	43.89
MS0037.2-0228	5.7	3.90	0.416	26.61	44.63	MS0136.3-2505	5.4	4.84	0.305	26.36	44.41
MS0037.7-0156	5.4	2.04	0.296	25.98	44.01	MS0136.3+0606	5.4	2.72	0.450	26.54	44.55
MS0038.0+3242	5.4	2.02	0.197	25.63	43.61	MS0136.8+3307	4.7	3.58	0.240	26.05	44.05
MS0038.7+3251	7.6	3.12	0.225	25.95	43.92	MS0139.3+0557	4.5	4.11	0.345	26.45	44.46
MS0038.8-0159	7.3	3.07	1.675	28.08	46.10	MS0140.3-3042	6.1	2.19	0.151	25.35	43.40
MS0039.0-0145	5.3	2.30	0.110	25.10	43.12	MS0144.2-0055	10.1	6.20	0.080	25.22	43.27
MS0039.2-0206	4.3	1.48	1.083	27.23	45.25	MS0148.4-3938	8.9	2.93	0.592	26.83	44.87
MS0048.8+2907	22.5	63.04	0.036	25.58	43.56	MS0149.5-3929	5.7	1.60	0.211	25.53	43.57
MS0049.9+0035	4.1	1.96	0.408	26.31	44.31	MS0150.6-1040	4.5	2.17	0.65:	26.80	44.84
MS0052.1+2931	7.2	7.32	0.151	25.94	43.92	MS0151.0-3919	4.1	1.69	0.350	26.04	44.09
MS0053.3-1035	5.0	3.33	0.308	26.25	44.26	MS0152.4+0424	6.2	6.28	1.132	27.93	45.93
MS0055.5+0014	4.1	3.21	2.095	28.39	46.40	MS0200.5-0857	5.5	2.74	0.218	25.80	43.84
MS0100.6+0205	6.8	5.33	0.392	26.68	44.70	MS0200.9-0858	5.0	2.41	0.773	27.04	45.08
MS0104.2+3153	6.3	4.35	2.027	28.51	46.49	MS0204.8+0217	4.8	1.86	0.673	26.80	44.81
MS0108.0+0139	4.4	5.64	0.713	27.34	45.36	MS0207.4-1016	4.2	2.67	1.970	28.21	46.24
MS0108.4+3836	6.9	2.98	0.353	26.36	44.34	MS0212.0+1741	4.8	3.23	0.160	25.67	43.62
MS0109.4+0242	4.8	3.76	0.266	26.15	44.17	MS0225.5+3121	7.3	14.11	0.058	27.19	45.22
MS0112.9-0132	10.6	4.95	0.120	25.54	43.54	MS0226.8-1041	5.8	2.53	0.620	26.83	44.86
MS0114.3-0123	4.2	2.77	0.559	26.78	44.79	MS0232.8-0400	6.4	7.19	1.450	28.26	46.29
MS0114.5+0809	5.9	2.71	1.486	27.89	45.89	MS0232.8-0400	6.9	5.07	0.376	26.61	44.64
MS0114.5-0140	4.4	1.81	0.388	26.22	44.22	MS0234.1+1620	6.8	3.86	0.158	25.74	43.68
MS0115.2+0812	4.1	1.04	0.35:	25.88	43.88	MS0234.8+0655	4.1	2.85	0.435	26.57	44.54
MS0116.6+3147	6.4	11.60	0.058	25.27	43.25	MS0237.6-0805	6.6	3.56	0.401	26.53	44.55
MS0116.7+0802	4.5	1.08	0.156	25.12	43.12	MS0237.9+0654	4.9	3.29	0.613	27.00	44.96
MS0117.2-2837	19.0	20.65	0.347	27.12	45.17	MS0238.8-2314	4.8	2.70	0.284	26.06	44.09
MS0120.0+0328	4.4	4.49	0.221	26.05	44.07	MS0242.3-4047	4.5	0.88	0.469	26.06	44.10
						MS0244.6-3020	5.3	2.68	0.530	26.68	44.71

TABLE 1—Continued

Source Name	S/N	Flux 0.3–3.5 keV	z	logLx 2 keV	logLx 0.3–3.5 keV	logLx 2 keV	logLx 0.3–3.5 keV	Source Name	S/N	Flux 0.3–3.5 keV	z	logLx 2 keV	logLx 0.3–3.5 keV
(1)	(2)	(3)	(4)	(5)	(6)	(5)	(6)	(1)	(2)	(3)	(4)	(5)	(6)
MS0244.8+1928	5.2	20.01	0.176	26.56	44.50	26.56	44.50	MS0459.5+0327	25.6	159.64	0.015	25.24	43.20
MS0302.5–2223	5.5	4.59	1.409	28.02	46.06	28.02	46.06	MS0506.3–5108	5.4	6.30	0.522	27.03	45.07
MS0310.4–5543	6.1	12.50	0.226	26.49	44.53	26.49	44.53	MS0516.6–4609	4.6	9.22	0.048	24.96	42.98
MS0311.8–0801	4.3	3.38	1.250	27.79	45.78	27.79	45.78	MS0521.7+7918	4.4	5.52	0.503	27.02	44.97
MS0312.0+1405	6.3	2.70	0.744	27.17	45.08	27.17	45.08	MS0526.7–3301	4.8	2.99	1.236	27.67	45.71
MS0317.9–1949	4.5	2.20	0.997	27.30	45.32	27.30	45.32	MS0530.6–1140	6.4	7.08	0.160	26.04	43.96
MS0318.0–1937	5.8	2.74	0.104	25.13	43.15	25.13	43.15	MS0536.3–2849	8.5	1.98	0.330	26.06	44.10
MS0321.5–6657	5.4	3.92	0.093	25.19	43.20	25.19	43.20	MS0536.5–2818	8.2	2.00	0.270	25.87	43.91
MS0325.2–1746	5.2	2.05	1.009	27.31	45.31	27.31	45.31	MS0537.4–2843	9.2	1.37	1.245	27.34	45.38
MS0330.8+0606	8.3	6.53	0.105	25.63	43.54	25.63	43.54	MS0700.7+6338	7.2	27.35	0.153	26.52	44.50
MS0331.1–0522	6.7	4.35	0.139	25.62	43.62	25.62	43.62	MS0713.4+3700	4.6	5.73	0.122	25.65	43.62
MS0334.2–3617	4.3	4.39	1.100	27.69	45.74	27.69	45.74	MS0719.9+7100	4.6	7.65	0.125	25.75	43.76
MS0335.4–2618	5.2	1.82	0.123	25.07	43.13	25.07	43.13	MS0721.2+6904	9.6	15.50	0.111	25.95	43.96
MS0336.3–2546	4.2	2.80	0.334	26.21	44.26	26.21	44.26	MS0731.6+8011	15.9	22.38	0.087	25.88	43.90
MS0339.8–2124	19.3	80.37	0.015	24.88	42.90	24.88	42.90	MS0737.0+7436	4.8	8.70	0.312	26.67	44.69
MS0340.3+0455	4.3	2.06	0.097	25.04	42.96	25.04	42.96	MS0740.4+3734	4.3	1.89	0.379	26.24	44.22
MS0340.9+0446	4.6	2.07	0.190	25.67	43.59	25.67	43.59	MS0745.1+5545	6.1	8.30	0.174	26.11	44.11
MS0341.9+0451	4.7	2.67	0.756	27.18	45.10	27.18	45.10	MS0754.6+3928	5.7	18.06	0.096	25.91	43.90
MS0357.4+1046	6.4	10.88	0.182	26.34	44.27	26.34	44.27	MS0801.9+2129	8.5	8.71	0.118	25.77	43.77
MS0358.3–3701	5.2	6.52	0.105	25.51	43.53	25.51	43.53	MS0803.3+7557	5.9	13.82	0.094	25.74	43.76
MS0358.3–3701	5.2	4.67	0.153	25.68	43.74	25.68	43.74	MS0806.6+2820	4.2	4.04	0.30	26.31	44.32
MS0402.0–3613	14.6	33.98	1.417	28.87	46.93	28.87	46.93	MS0807.0+7426	4.4	1.26	0.393	26.05	44.08
MS0412.4–0802	12.6	27.25	0.037	25.24	43.22	25.24	43.22	MS0807.7+7453	5.7	1.79	0.581	26.61	44.64
MS0414.7–6315	4.1	2.42	0.614	26.81	44.83	26.81	44.83	MS0808.0+4840	4.8	2.97	0.700	27.06	45.06
MS0420.8–3904	9.5	2.43	0.271	25.96	44.00	25.96	44.00	MS0809.9+4809	5.0	2.25	0.459	26.49	44.49
MS0423.8–1247	4.1	1.87	0.161	25.39	43.39	25.39	43.39	MS0815.7+5233	4.5	3.15	0.624	26.96	44.96
MS0438.6–1050	5.3	3.48	0.868	27.39	45.37	27.39	45.37	MS0818.8+5428	8.9	12.42	0.086	25.63	43.63
MS0439.0+0158	6.2	7.60	0.196	26.24	44.18	26.24	44.18	MS0822.0+0309	5.4	1.46	0.577	26.53	44.54
MS0439.7–4319	12.0	12.61	0.593	27.48	45.51	27.48	45.51	MS0822.1+2644	5.6	3.20	0.246	26.02	44.02
MS0440.0–1058	4.5	4.29	0.279	26.29	44.27	26.29	44.27	MS0824.2+0327	4.1	0.92	1.431	27.37	45.38
MS0444.9–1000	4.1	2.50	0.095	25.05	43.03	25.05	43.03	MS0828.7+6614	4.3	2.48	0.610	26.83	44.83
MS0447.1–0917	4.8	2.58	0.946	27.35	45.33	27.35	45.33	MS0828.7+6601	7.0	4.90	0.329	26.49	44.49
MS0449.4–1823	5.4	8.40	0.338	26.75	44.75	26.75	44.75	MS0829.4+1106	4.2	4.24	0.453	26.75	44.75
MS0450.3–1817	4.6	5.25	0.059	24.92	42.92	24.92	42.92	MS0829.9+0455	4.7	5.16	0.295	26.39	44.41
MS0457.9+0141	5.9	13.52	0.128	26.07	44.03	26.07	44.03	MS0830.3+2828	4.2	1.97	0.283	25.94	43.95
MS0457.9–0556	5.5	4.65	0.303	26.40	44.39	26.40	44.39	MS0832.6+6449	7.4	3.91	0.271	26.20	44.20

TABLE 1—Continued

Source Name (1)	S/N (2)	Flux keV (3)	z (4)	LogLx keV (5)	LogLx keV (6)	Source Name (1)	S/N (2)	Flux keV (3)	z (4)	LogLx keV (5)	LogLx keV (6)
MS0832.8+5815	4.9	1.59	0.358	26.09	44.09	MS0942.8+0950	17.8	42.31	0.013	24.47	42.49
MS0833.3+6523	8.9	3.84	1.112	27.70	45.69	MS0944.1+1333	10.0	38.98	0.131	26.50	44.51
MS0838.2+1345	5.2	1.99	1.10:	27.39	45.40	MS0950.2+0804	4.9	2.52	1.451	27.81	45.83
MS0838.6+1325	5.6	1.73	0.723	26.86	44.86	MS0952.3+4412	5.2	5.41	0.465	26.83	44.88
MS0840.2+1906	5.1	1.84	0.274	25.86	43.89	MS0957.0+6856	4.7	1.97	0.500	26.51	44.52
MS0840.8+2629	5.0	9.02	0.258	26.51	44.52	MS0958.4+6913	5.7	2.68	0.928	27.32	45.33
MS0841.7+1628	4.6	5.55	0.150	25.77	43.79	MS1003.6+1300	5.3	2.75	0.648	26.93	44.94
MS0842.7-0720	6.0	6.14	0.144	25.78	43.80	MS1006.3+8212	4.4	3.11	2.410	28.57	46.58 (1)
MS0844.9+1836	7.4	9.21	0.086	25.48	43.50	MS1006.7+8145	5.4	4.34	0.630	27.10	45.11
MS0845.1+3751	4.2	4.20	0.307	26.34	44.36	MS1011.0+5708	4.5	1.86	0.568	26.57	44.63
MS0847.5+2813	7.8	3.72	0.330	26.36	44.37	MS1018.2+2010	4.1	8.76	0.250	26.44	44.47
MS0849.0+2845	6.7	1.73	1.273	27.49	45.51	MS1018.5+4830	4.8	3.46	0.232	25.95	44.00
MS0849.2+2829	7.3	1.72	0.209	25.58	43.60	MS1019.0+4836	4.3	2.70	0.062	24.62	42.68
MS0849.5+0805	28.1	101.44	0.062	26.26	44.25	MS1019.7-1027	4.0	3.04	0.254	26.04	44.03
MS0849.7+2015	9.9	4.47	0.449	26.74	44.76	MS1020.2+6850	4.4	2.86	0.078	24.87	42.91
MS0849.8+2820	6.4	1.55	0.197	25.48	43.49	MS1022.8+6844	4.2	1.90	0.421	26.29	44.33
MS0850.0+2827	4.1	0.84	1.273	27.18	45.20	MS1030.2-2757	6.0	14.60	0.148	26.21	44.20
MS0850.2+1336	4.8	11.40	0.194	26.34	44.35	MS1044.2+3531	4.5	3.44	0.370	26.41	44.45
MS0850.2+2825	6.0	1.37	0.922	27.01	45.03	MS1045.1+3450	5.1	3.63	0.203	25.85	43.89
MS0850.8+1401	6.0	9.44	0.194	26.25	44.26 (1)	MS1046.1+1411	7.0	3.90	0.290	26.25	44.27
MS0854.2+0543	4.5	10.13	0.153	26.07	44.07	MS1046.2+1442	5.6	4.61	0.453	26.76	44.79
MS0904.4-1505	10.2	10.44	0.054	25.16	43.14	MS1047.0+3537	7.0	6.24	0.161	25.87	43.91
MS0905.6-0817	4.5	6.85	0.071	25.20	43.20	MS1047.3+3518	10.4	9.21	0.040	24.78	42.82
MS0906.3+1111	8.7	17.19	0.160	26.34	44.34	MS1050.9+5418	4.3	4.89	0.995	27.61	45.67
MS0919.3+5133	8.3	7.73	0.161	25.95	44.00	MS1053.5-0310	4.4	1.11	0.184	25.28	43.29
MS0919.9+4543	4.3	11.92	0.293	26.71	44.76	MS1053.8-0354	7.7	3.48	0.452	26.65	44.66
MS0921.8+3451	4.7	1.68	0.487	26.38	44.42	MS1053.9-0332	4.4	0.86	0.626	26.39	44.40
MS0921.9+3920	7.8	3.85	0.245	26.05	44.10	MS1054.8-0335	8.5	1.11	0.835	26.82	44.83 (1)
MS0922.7+3420	8.0	6.39	0.158	25.86	43.90	MS1055.1-0400	4.8	2.62	0.550	26.73	44.74
MS0925.1-0605	4.4	1.62	0.834	26.97	44.99	MS1058.8+1003	5.0	3.06	0.487	26.68	44.68
MS0930.9+2128	5.2	5.36	0.172	25.89	43.91	MS1059.0+7302	9.3	13.58	0.089	25.68	43.70
MS0937.8+1153	7.2	2.14	0.783	27.02	45.04	MS1100.3+4507	4.5	1.13	1.013	27.00	45.05
MS0938.1-2340	6.4	1.57	0.200	25.52	43.51 (1)	MS1105.4+3747	4.1	2.02	0.480	26.45	44.49
MS0939.2+1212	4.0	1.00	0.997	26.96	44.98 (1)	MS1108.3+3530	5.5	5.34	0.061	24.92	42.96
MS0939.8+0952	4.8	5.90	0.205	26.09	44.11	MS1109.2+3814	4.4	3.10	0.720	27.07	45.11
MS0941.7-2348	4.5	1.03	0.615	26.46	44.46						

TABLE 1—Continued

Source Name		S/N	Flux		z	LogLx		LogLx				
(1)	(1)	(2)	0.3–3.5	3–3.5	(3)	(4)	2	2	0.3–3.5			
			keV	keV			keV	keV	keV			
			(3)	(5)	(4)	(4)	(5)	(5)	(6)			
MS1109.3+3544		4.9	3.04	0.909	0.030	27.32	45.36	4.7	4.64	0.053	24.72	42.77
MS1110.3+2210		9.5	5.23	0.030	0.076	24.26	42.32	12.6	16.28	0.087	25.72	43.76
MS1112.5+4059		14.1	15.45	0.076	0.092	25.58	43.62	4.3	3.72	0.263	26.11	44.15
MS1114.4+1801		4.6	1.02	0.092	0.092	24.56	42.61	4.0	2.78	1.416	27.80	45.84
MS1115.3+1824		4.5	0.97	0.644	0.644	26.43	44.48	7.3	3.61	0.271	26.12	44.17
MS1134.7–0900		4.1	2.24	0.932	0.932	27.24	45.26	5.1	5.87	0.305	26.46	44.49
MS1136.5+3413		14.1	48.71	0.032	0.032	25.31	43.35	6.6	3.96	1.843	28.28	46.33
MS1138.1+0400		4.2	2.81	0.098	0.098	25.07	43.11	4.5	1.78	0.425	26.26	44.31
MS1138.6+6553		4.7	1.26	0.805	0.805	26.78	44.84	4.1	1.14	0.295	25.71	43.75 (1)
MS1139.7+1040		6.8	12.08	0.150	0.150	26.12	44.13	5.2	2.28	0.158	25.42	43.45
MS1142.4+6610		4.4	1.88	0.328	0.328	26.02	44.07	5.7	0.94	0.420	25.98	44.02
MS1143.5–0411		8.6	9.06	0.133	0.133	25.87	43.89	4.7	2.61	0.187	25.65	43.67
MS1143.5–1643		4.2	2.01	1.357	1.357	27.64	45.65	4.1	2.13	0.261	25.87	43.89
MS1148.3+7125		4.9	8.98	0.114	0.114	25.70	43.75	5.1	2.46	0.160	25.46	43.50
MS1152.9+2344		5.8	7.37	0.136	0.136	25.79	43.83	4.1	2.63	1.375	27.73	45.78
MS1156.5+5323		6.5	4.03	0.482	0.482	26.75	44.79	6.0	5.89	0.281	26.36	44.42
MS1200.1–0330		4.0	64.01	0.020	0.020	25.02	43.05	4.1	4.23	0.111	25.36	43.40
MS1200.2–1829		4.6	2.37	0.065	0.065	24.63	42.66	5.0	2.90	1.122	27.56	45.58
MS1205.7+6427		9.5	5.92	0.105	0.105	25.46	43.49	4.2	1.88	0.346	26.07	44.12
MS1214.3+3811		11.9	4.42	0.062	0.062	24.85	42.89	8.5	7.15	0.112	25.59	43.63
MS1214.7+2806		7.9	4.06	0.394	0.394	26.55	44.59	5.0	3.46	0.402	26.50	44.54
MS1215.2+2847		4.4	1.49	2.830	2.830	28.44	46.48	6.8	5.12	0.450	26.78	44.83
MS1215.9+3005		21.4	81.49	0.013	0.013	24.73	42.78	9.0	6.40	0.329	26.59	44.61
MS1216.3+0216		4.7	4.89	0.327	0.327	26.44	44.48	4.5	2.90	0.135	25.36	43.41
MS1217.0+0700		5.9	8.81	0.080	0.080	25.37	43.42	4.9	5.33	0.431	26.77	44.80
MS1217.4+7549		7.6	2.83	0.464	0.464	26.58	44.60	4.8	4.12	0.072	24.94	42.99
MS1218.6+7522		8.7	3.32	0.643	0.643	26.99	45.01	4.0	2.40	0.986	27.29	45.35
MS1219.0+7528		4.0	1.00	1.259	1.259	27.24	45.26 (1)	6.1	7.20	0.090	25.38	43.44
MS1219.6+7535		24.8	106.43	0.071	0.071	26.38	44.39	7.8	14.17	0.241	26.59	44.65
MS1220.9+1601		5.3	6.81	0.081	0.081	25.29	43.32	6.9	6.15	0.311	26.47	44.53
MS1223.5+2522		6.6	5.58	0.067	0.067	25.02	43.06	4.6	7.96	0.107	25.58	43.64
MS1224.7+6733		4.4	7.03	0.153	0.153	25.88	43.91	8.7	2.87	0.136	25.38	43.42
MS1232.4+1550		6.9	17.77	0.046	0.046	25.20	43.23	4.6	3.05	0.082	24.98	42.98 (1)
MS1233.3+7426		5.7	2.90	0.084	0.084	24.94	42.98	4.4	3.79	0.266	26.13	44.17
MS1234.9+6651		4.6	5.39	0.860	0.860	27.51	45.54	4.0	4.88	0.905	27.51	45.56

TABLE 1—Continued

Source Name (1)	S/N (2)	Flux 0.3-3.5 key (3)	z (4)	LogLx 2 0.3-3.5 key (5)	LogLx 2 0.3-3.5 key (6)	Source Name (1)	S/N (2)	Flux 0.3-3.5 key (3)	z (4)	LogLx 2 0.3-3.5 key (5)	LogLx 2 0.3-3.5 key (6)
MS1342.8+6016	4.2	3.51	0.474	26.68	44.72	MS1516.3+7203	4.0	1.45	0.491	26.33	44.37 (1)
MS1351.6+4005	8.0	8.08	0.062	25.09	43.15	MS1519.8-0633	7.0	22.23	0.083	25.89	43.85
MS1357.5-0227	4.2	5.53	0.416	26.77	44.78	MS1525.1-1551	6.1	14.12	0.230	26.58	44.60
MS1359.1+0430	8.9	12.59	0.163	26.19	44.23	MS1541.0-1101	4.1	3.91	0.329	26.47	44.39
MS1402.3+2627	4.7	3.71	0.585	26.91	44.96	MS1545.3+0305	5.5	6.73	0.098	25.51	43.49
MS1403.5+5439	8.0	4.67	0.082	25.11	43.17	MS1549.8+2022	12.6	13.66	0.250	26.66	44.67
MS1408.1+2617	4.3	5.25	0.072	25.05	43.10	MS1555.1+4522	4.1	4.51	0.180	25.82	43.87
MS1412.8+1320	4.8	2.48	0.139	25.33	43.37	MS1558.0+4123	4.5	1.80	1.168	27.37	45.42
MS1413.8+1400	8.6	8.92	0.141	25.89	43.94	MS1558.3+4138	5.0	1.47	0.368	26.03	44.08
MS1414.0+0130	5.1	6.85	0.142	25.81	43.83	MS1559.1+3324	4.1	2.91	0.087	24.98	43.01
MS1414.2+0140	4.3	5.56	0.466	26.87	44.90	MS1559.4+4122	4.0	1.00	0.623	26.41	44.46 (1)
MS1414.8-1247	4.3	7.22	0.198	26.20	44.17	MS1559.8+4202	4.3	1.58	0.759	26.82	44.87
MS1414.9+1337	4.7	2.52	0.088	24.92	42.96	MS1601.1+4119	4.6	1.17	0.534	26.31	44.36 (2)
MS1415.4+5640	9.1	8.96	0.150	25.95	44.00	MS1601.9+4125	4.1	1.27	0.299	25.73	43.78 (1)
MS1416.3-1257	14.0	58.78	0.129	26.71	44.68	MS1611.8-0323	5.4	6.16	0.298	26.55	44.49
MS1417.0+0345	4.0	2.76	0.189	25.67	43.71	MS1613.3+3105	9.8	2.78	0.141	25.41	43.44
MS1420.1+2956	8.6	7.16	0.053	24.91	42.96	MS1613.6+3055	8.2	2.14	1.087	27.38	45.41
MS1421.5+6321	8.2	5.27	0.160	25.79	43.83	MS1614.1+3239	4.9	2.73	0.118	25.23	43.26
MS1425.7+6320	4.1	1.74	0.358	26.08	44.13 (1)	MS1614.9+3052	7.3	2.14	0.270	25.91	43.94
MS1426.5+0130	20.5	53.01	0.086	26.24	44.26	MS1617.9+1731	8.8	21.13	0.116	26.14	44.14
MS1426.9+1052	10.2	4.98	1.833	28.38	46.42	MS1623.4+2712	10.6	7.78	0.525	27.15	45.17
MS1427.4+1034	4.6	1.78	0.239	25.70	43.74	MS1628.5+2140	5.1	3.71	0.087	25.12	43.12
MS1430.4+0527	7.9	6.48	0.202	26.11	44.14	MS1633.1+2643	4.3	0.98	1.336	27.31	45.32 (1)
MS1431.5+0526	5.5	3.14	0.152	25.53	43.56	MS1640.0+3940	5.5	4.39	0.540	26.89	44.95
MS1437.5+2829	4.4	6.38	0.386	26.72	44.76	MS1644.1-0258	4.3	3.36	0.259	26.15	44.09
MS1442.8+6344	4.1	2.93	1.380	27.79	45.84	MS1657.1+3524	4.4	1.11	0.949	26.93	44.97
MS1451.5+2139	5.0	2.86	0.102	25.13	43.15	MS1701.5+6102	13.0	3.32	0.164	25.62	43.65
MS1455.7+2121	9.9	11.76	0.080	25.52	43.54	MS1701.7+4914	4.7	3.91	0.538	26.86	44.89
MS1456.4+2147	9.9	12.61	0.062	25.33	43.35	MS1703.2+6049	6.8	0.98	0.284	25.62	43.65
MS1500.5+2552	6.7	7.37	0.191	26.13	44.14	MS1703.5+6052	7.4	1.13	1.358	27.37	45.40
MS1503.0+2606	6.4	2.25	0.169	25.50	43.51	MS1703.7+2417	10.6	8.29	0.113	25.71	43.71
MS1503.2+7406	4.4	2.43	0.169	25.52	43.55	MS1705.5+5443	5.0	5.54	0.102	25.41	43.44
MS1503.9-1634	5.1	10.46	0.299	26.77	44.73	MS1709.6+4823	4.6	6.83	0.174	25.99	44.02
MS1512.4+2551	6.5	3.37	0.246	26.04	44.04	MS1710.8+1624	6.6	5.67	0.187	26.04	44.01
MS1513.6+3358	4.8	3.77	0.145	25.55	43.59	MS1718.6+4902	5.0	4.23	0.198	25.90	43.94
MS1513.7+1948	7.2	8.12	0.384	26.85	44.86	MS1719.4+3239	4.3	2.24	0.838	27.12	45.13

TABLE 1—Continued

Source Name (1)	S/N (2)	Flux 0.3–3.5 keV (3)	z (4)	LogLx keV (5)	LogLx keV (6)	Source Name (1)	S/N (2)	Flux 0.3–3.5 keV (3)	z (4)	LogLx keV (5)	LogLx keV (6)
MS1727.8+5159	5.1	12.25	0.129	25.98	44.00	MS2204.0-4059	11.8	11.49	0.231	26.47	44.52
MS1739.8+6712	4.3	7.95	0.118	25.73	43.73	MS2209.8+1800	4.6	11.40	0.082	25.56	43.55
MS1745.2+2747	6.6	3.30	0.156	25.61	43.60	MS2210.2+1827	7.5	15.50	0.079	25.66	43.65
MS1746.2+6738	5.3	21.94	0.041	25.22	43.22	MS2215.2-0347	6.8	14.92	0.242	26.69	44.67
MS1747.2+6837	9.0	18.42	0.063	25.53	43.52	MS2222.5+2114	4.4	3.44	0.617	26.99	44.98
MS1754.5+7017	5.1	11.13	0.062	25.30	43.29	MS2222.9+2046	5.0	4.33	0.139	25.62	43.61
MS1803.6+6738	12.5	33.81	0.136	26.49	44.49	MS2223.0+2110	4.8	3.50	0.310	26.29	44.29
MS1804.8-6556	6.7	14.67	0.180	26.43	44.39	MS2223.6-0517	5.4	2.38	1.866	28.14	46.12
MS1806.5+6939	4.1	1.08	0.461	26.19	44.17	MS2224.1+2056	5.0	3.95	0.261	26.17	44.17
MS1818.7+6740	4.9	11.74	0.310	26.83	44.81	MS2232.6-3743	4.2	7.00	0.198	26.10	44.15
MS1837.8+4538	4.0	3.60	0.958	27.51	45.49	MS2247.8-0703	5.2	3.82	1.710	28.21	46.22
MS1846.5-7857	5.3	13.14	0.029	24.74	42.69	MS2248.7-0727	8.0	7.18	0.315	26.60	44.61
MS1849.2-7832	4.2	7.48	0.042	24.82	42.77	MS2252.2+1126	6.5	11.49	0.028	24.61	42.60
MS1906.5-6421	5.5	2.30	0.371	26.31	44.28	MS2254.1+0712	8.8	9.03	0.146	25.99	43.98
MS1912.5+6719	5.5	2.71	0.394	26.44	44.41	MS2254.5+0209	11.7	8.59	0.105	25.67	43.65
MS1955.9-3516	7.7	7.03	0.233	26.34	44.31	MS2254.9-3712	11.6	24.55	0.039	25.17	43.22
MS2007.8-3622	8.6	16.37	0.177	26.44	44.42	MS2255.0-3651	4.1	2.40	0.336	26.15	44.20
MS2017.3-1441	4.3	4.49	0.550	26.99	44.98	MS2302.8-2319	4.4	3.71	0.651	27.04	45.07
MS2034.5-2253	4.9	7.62	0.256	26.43	44.44	MS2304.1-4418	5.1	4.10	0.175	25.77	43.81
MS2037.3-0035	4.6	2.21	0.609	26.81	44.78	MS2307.9-4328	4.4	4.52	0.055	24.76	42.79
MS2039.5-0107	6.4	3.53	0.142	25.58	43.55	MS2316.9+0019	4.6	5.42	0.118	25.54	43.56
MS2044.1+7532	5.2	2.36	0.184	25.70	43.61	MS2318.2-4220	7.6	2.85	0.212	25.79	43.83
MS2053.2-0503	8.6	7.88	0.281	26.55	44.54	MS2329.3-3827	4.1	3.08	1.195	27.64	45.68
MS2113.8+0455	4.1	2.53	1.001	27.42	45.39	MS2338.9-1206	4.0	2.80	0.085	24.96	42.98
MS2118.4-1050	5.7	2.32	0.092	24.97	42.97	MS2340.9-1511	7.8	16.35	0.137	26.14	44.18
MS2125.9-1456	6.2	2.06	0.304	26.05	44.04	MS2348.3+3250	4.1	7.38	0.090	25.47	43.45
MS2128.3+0349	8.9	24.05	0.094	26.01	44.00	MS2348.6+1956	8.3	6.31	0.043	24.72	42.72
MS2134.0+0018	4.3	1.57	0.805	26.93	44.93	MS2353.9+0714	4.0	3.87	0.342	26.44	44.43
MS2134.0+0028	6.3	8.67	1.936	28.74	46.73	MS2356.1-6358	4.4	5.17	0.163	25.81	43.84
MS2134.1-1518	6.2	4.42	0.178	25.86	43.85	MS2357.4-3520	4.1	2.23	0.508	26.54	44.59
MS2136.0-2307	4.3	7.76	0.646	27.38	45.39	MS2357.5-6352	7.5	12.28	0.136	26.01	44.05
MS2141.2+1730	4.0	8.94	0.213	26.37	44.33						
MS2143.2+1429	4.5	1.91	1.387	27.69	45.66						
MS2144.9-2012	5.3	5.72	0.102	25.43	43.45						
MS2154.5+0107	4.2	2.19	0.220	25.77	43.75						
MS2159.5-5713	10.6	11.53	0.083	25.54	43.57						

NOTES.—(1) Source listed as class 1 in Gioia et al. 1990; (2) source listed as class 2 in Gioia et al. 1990; (3) source listed as star in Gioia et al. 1990; (4) source listed as cluster in Gioia et al. 1990.

TABLE 2
COMPOSITION OF THE EMSS AS A FUNCTION OF THE SURVEY FLUX LIMIT

Sky flux Limit *E-13 erg cm s	Area (deg)	AGN in EMSS	UNID. in EMSS	UNID. in EMSS (Class 1)	(GAL,BL,CL) in EMSS	Total Sources in EMSS with flux >= Slim
0.508	0.0896	427	31	27	161	835
0.609	0.7176	427	29	26	161	832
0.731	2.535	427	29	26	161	832
0.825	4.654	427	26	23	161	829
0.878	6.368	425	26	23	161	825
1.05	15.05	413	24	21	160	808
1.26	29.38	404	20	18	159	786
1.52	55.22	394	18	16	157	758
1.82	94.24	373	15	14	153	720
2.18	139.4	344	10	9	147	669
2.62	191.6	308	6	5	133	600
3.14	249.5	260	4	3	125	520
3.77	319.1	224	2	2	113	455
4.53	402.0	183	1	1	106	390
5.43	497.0	153	1	1	93	331
6.52	582.9	125	1	1	88	285
7.83	657.7	94	1	1	81	229
9.39	711.8	70	1	1	73	179
11.3	743.7	63	0	0	66	157
13.5	762.7	45	0	0	58	127
16.2	771.9	32	0	0	47	99
19.5	775.7	25	0	0	42	83
23.4	777.4	18	0	0	32	62
28.0	777.9	14	0	0	27	49
33.6	778.1	14	0	0	21	42

NOTE.—Total area = 778.1 square degrees.

the “expected” AGNs are distributed over the broad range of observed luminosities.

Finally, Figure 4 shows the $\log z$ - $\log L_x$ plane and how it is populated by the present sample. The dotted lines represent

the limiting sensitivities $S_{\text{lim}} = 5.08 \times 10^{-14}$ ergs cm^{-2} s^{-1} and $S_{\text{lim}} = 2 \times 10^{-12}$ ergs cm^{-2} s^{-1} . Note that at these flux limits ~ 0.1 and 776 square degrees of sky have been surveyed, respectively (see Table 2).

The number of objects at our disposal is much larger than the number used by Maccacaro, Gioia, & Stocke (1984), and it is of the same order as the largest complete samples of optically selected quasars currently available (e.g., Boyle et al. 1990). It is thus possible to study the luminosity function in different redshift shells. However, inspection of Figure 4 also reveals the limitations of the application of this approach to our data set. The low-luminosity end (10^{42} – 10^{44} ergs s^{-1}) of the luminosity function is sampled only at $z \lesssim 0.3$, while the high-luminosity end (10^{45} – 10^{47} ergs s^{-1}) is sampled only at $z \gtrsim 0.5$. Therefore, in studying the luminosity function, we shall follow two approaches: first we will derive the observed luminosity function in different redshift shells without using any evolutionary model. Then we will use an evolutionary model, determine its best-fit parameters, and derive the “de-evolved” luminosity function for the whole sample.

3. THE OBSERVED X-RAY LUMINOSITY FUNCTION

A nonparametric representation of the observed X-ray luminosity function is obtained using the $1/V_a$ method of Avni & Bahcall (1980), a generalization of the $1/V_{\text{max}}$ method (Schmidt 1968) when several samples are analyzed.

The procedure used to derive the X-ray luminosity function in different redshift shells (defined by z_{low} – z_{high}) is as follows. For each AGN falling in the shell z_{low} – z_{high} , and each limiting sensitivity, we have computed the maximum redshift at which

TABLE 3
RELEVANT DATA FOR THE SAMPLE OF 21 “EXPECTED” AGNs INCLUDED
IN THE STATISTICAL ANALYSIS

Source Name	S/N	Flux 0.3–3.5 keV	z	logL _x 2 keV	logL _x 0.3–3.5 keV
(1)	(2)	(3)	(4)	(5)	(6)
MS0134.4+2043	4.1	1.12	0.450	26.19	44.17
MS0317.7–6647	13.9	10.88	0.050	25.08	43.09
MS0354.2–3658	4.1	3.09	0.150	25.48	43.54
MS0358.0–2355	4.4	3.84	0.050	24.61	42.64
MS0405.4–5625	4.5	2.06	0.250	25.82	43.85
MS0407.3–5551	5.3	2.40	0.950	27.28	45.31
MS0418.5–6240	4.9	2.44	0.650	26.88	44.89
MS0420.0–3838	4.4	0.82	0.350	25.74	43.78
MS0421.3–3916	4.3	1.12	0.250	25.54	43.58
MS0422.3–3838	4.6	1.11	0.350	25.87	43.91
MS0501.0–2237	4.8	3.26	1.050	27.53	45.56
MS0623.1–5223	4.6	1.81	1.050	27.32	45.30
MS0625.5–5532	4.7	1.86	0.350	26.15	44.13
MS1610.4+6616	4.4	2.34	0.150	25.40	43.42
MS1613.0+3053	4.6	1.04	0.450	26.10	44.13
MS1703.2+6100	5.0	0.76	1.050	26.89	44.92
MS1704.6+6053	4.1	0.55	0.350	25.57	43.60
MS1903.9–6353	4.8	1.35	0.950	27.08	45.06
MS1907.8–6406	5.4	1.87	0.450	26.41	44.39
MS2223.8–0503	4.3	1.77	0.150	25.31	43.30
MS2310.9–4948	4.0	1.40	0.350	25.96	44.01

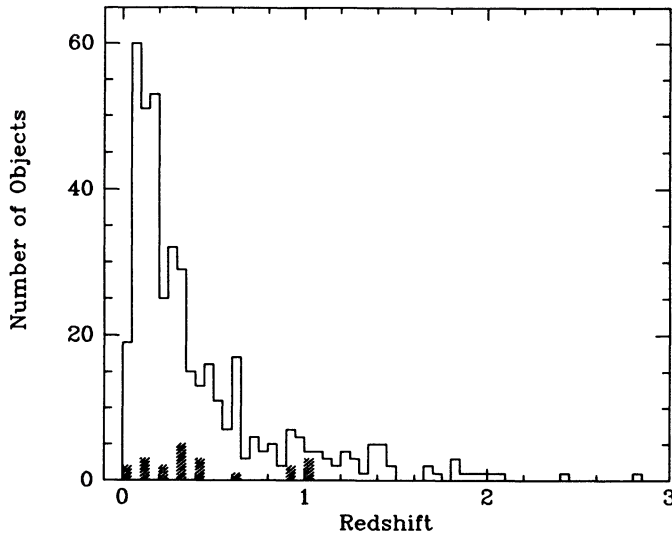


FIG. 2.—Redshift distribution of the 427 spectroscopically classified AGNs. The shaded area indicates the distribution of the 21 “expected” AGNs included in the statistical analysis (see § 2). The histogram bin size is 0.05.

the source can be detected. This, combined with the solid angle of sky searched at that given limiting sensitivity, gives the volume available. The fraction of this volume contained in the volume defined by the redshift shell under consideration is retained, and all the volumes are summed to obtain the total volume searched, V_S . The contribution of each AGN to the luminosity function in each redshift shell considered is then given by $1/V_S$.

The integral luminosity function is then obtained by summing, in order of decreasing luminosity, the individual values of $1/V_S$, i.e.,

$$N(>L) = \sum_{j:L_j>L} \frac{1}{V_S},$$

over all the objects with luminosity greater than L .

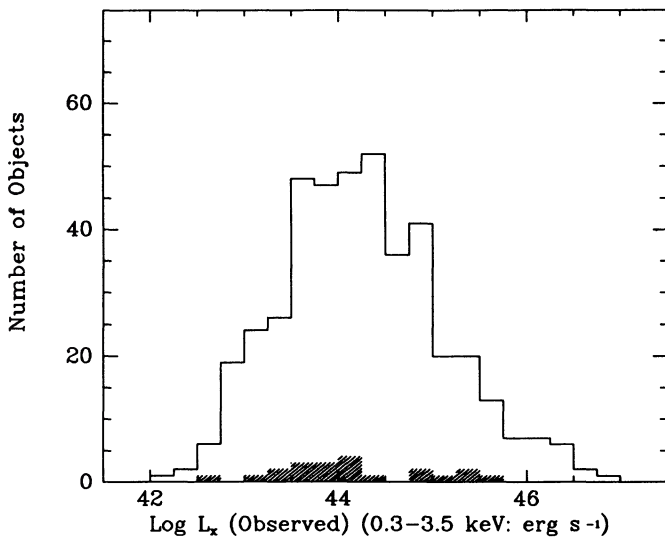


FIG. 3.—The 0.3–3.5 keV observed X-ray luminosity distribution of the 427 spectroscopically classified AGNs. The shaded area indicates the distribution of the 21 “expected” AGNs (see § 2). Data have been binned in bins of equal logarithmic width of 0.25.

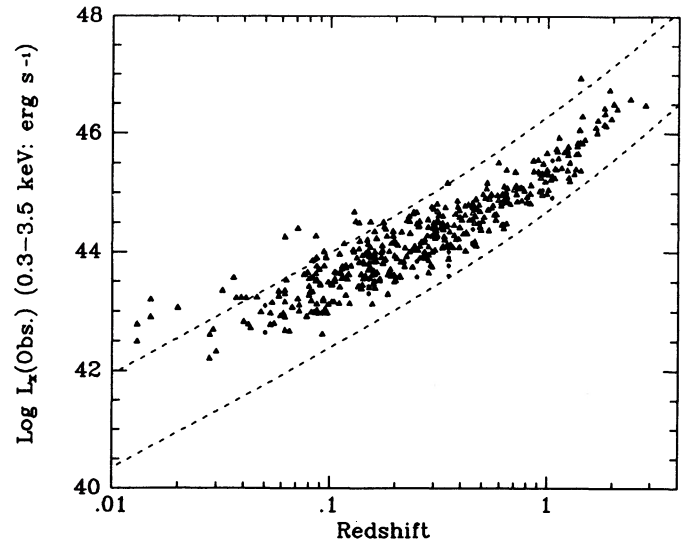


FIG. 4.—The 448 AGNs (427 “observed” AGNs [open triangles] + 21 “expected” AGNs [filled circles]) plotted in the $\log z$ – $\log L_x$ plane. The plotted L_x is the observed X-ray luminosity in the 0.3–3.5 keV band. The two dotted lines represent the limiting sensitivities $S_{\text{lim}} = 5.08 \times 10^{-14}$ and $S_{\text{lim}} = 2 \times 10^{-12}$ ergs $\text{cm}^{-2} \text{s}^{-1}$.

In order to obtain the differential X-ray luminosity function (hereafter XLF), we bin the individual contributions in bins of equal logarithmic width $\Delta \log L$. For each bin we have

$$\frac{dN(L)}{dL} = \sum_{i=1}^n \frac{1}{V_{S_i} \Delta L},$$

where n is the number of objects in that bin. Errors (1σ) have been determined from the number of objects contributing to each bin and have been computed using Poisson statistics.

Using this procedure and setting $z_{\text{low}} = 0$ and $z_{\text{high}} = 0.1$, we can determine the AGN local differential luminosity function.

3.1. The Local Luminosity Function

There are 81 AGNs with $z \leq 0.1$. They cover the luminosity range 1.6×10^{42} to 2.5×10^{44} ergs s^{-1} . These sources have been used to derive the local XLF shown in Figure 5 (filled circles). Data have been binned in bins of equal logarithmic width of 0.30.¹⁰

Since the local XLF shows a substantial curvature, we have not attempted a fit with a single power law.

The luminosity function shown in Figure 5 is the 0.3–3.5 keV local luminosity function obtained from objects selected and measured in this same energy band. It can be compared with other X-ray luminosity functions obtained either directly or indirectly (e.g., from optical data plus a knowledge of the ratio of the optical to the X-ray luminosity).

A direct estimate of the local AGN XLF was obtained using the *HEAO 1 A-2* data by Piccinotti et al. (1982). Since then, the optical identification of a number of *HEAO 1 A-2* sources has been revised, and the AGN sample of Piccinotti et al. (1982) has been updated by Danese et al. (1986). We have used the AGN sample as defined by Danese et al. (1986) to rederive the AGN XLF.

¹⁰ The bin width of 0.30 is chosen so as to prevent the occurrence of empty bins. We note that in the rest of the analysis, since more objects are available, we have chosen a bin width of 0.25.

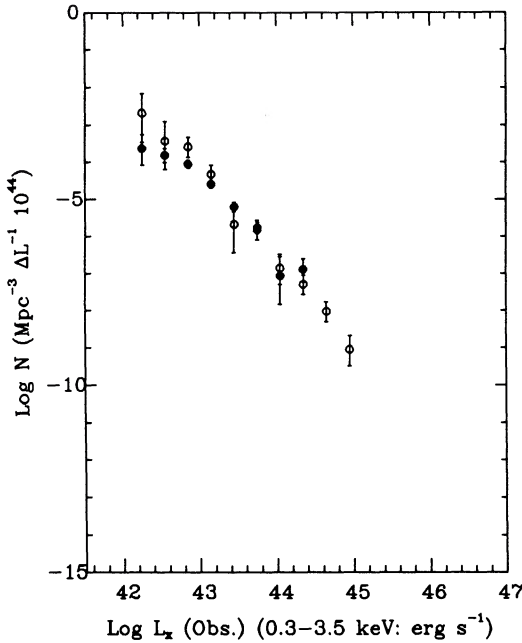


FIG. 5.—Differential local X-ray luminosity function ($z \leq 0.1$) (filled circles). The open circles indicate the *HEAO 1 A-2* local luminosity function obtained as explained in § 3.1. Data have been binned in bins of equal logarithmic width of 0.30; 1σ error bars are determined by the number of objects which contribute to each bin.

In order to compare the A-2 local XLF with our local XLF, we have converted the *HEAO 1 A-2* count rate (R15 counts s^{-1}) reported in Piccinotti et al. (1982) to fluxes in the 0.3–3.5 keV energy band. To do this, we have assumed an average conversion factor $1 \text{ R15 counts } s^{-1} = 2.19 \times 10^{-11} \text{ ergs cm}^{-2} s^{-1}$ in the 2–10 keV band (appropriate for an energy index of 0.65; see Table 1 in Della Ceca et al. 1990). The same spectral index $\alpha = 0.65$ was then adopted to convert 2–10 keV fluxes to 0.3–3.5 keV fluxes. The local *HEAO 1* XLF obtained in this manner is shown in Figure 5 (open circles). For ease of comparison, data have been binned in bins of equal logarithmic width of 0.30, the same bin width used for the EMSS XLF. The two luminosity functions show good agreement for luminosities greater than $\sim 2 \times 10^{43} \text{ ergs } s^{-1}$, where they are both well described by a single power law; at lower luminosities the XLF obtained from the EMSS AGN sample is flatter than the XLF obtained from the harder *HEAO 1 A-2* data.

Intrinsic absorption in low-luminosity objects may be responsible for this difference, since it would affect the EMSS sources (selected in the 0.3–3.5 keV band) more than the *HEAO 1* sources (selected in a higher energy band). If this is indeed the case, then we expect to see an even more pronounced low-luminosity flattening in the luminosity function of AGNs selected by “softer” X-ray telescopes like those of *EXOSAT* or *ROSAT*. Stocke et al. (1991) find evidence for obscuration in the optical spectra of a number of AGNs of the present sample through the presence of a strong Balmer decrement.

Intrinsic absorption in AGNs was also suggested by Warwick & Stewart (1990) as the possible cause of the apparent deficiency of sources in the EMSS with respect to the prediction of a fluctuation analysis of *Ginga* data.

The detection of very low luminosity AGNs and the extension of the local XLF to luminosities below $10^{42} \text{ ergs } s^{-1}$ are very difficult tasks. Normal galaxies are known to be sources of X-ray emission with luminosities in the range $\sim 10^{38} - 10^{42} \text{ ergs } s^{-1}$ (see Fabbiano 1989 for a recent review on X-ray emission from normal galaxies, and see Stocke et al. 1991 for the X-ray properties of X-ray-selected normal galaxies). These luminosities are the results of integrated emission from individual sources (e.g., supernova remnants, galactic binaries, star-forming regions, etc.) and/or diffuse emission from hot gas. In order to extend the study of the X-ray emission from active galactic nuclei to luminosities of the same order as those typical of the host galaxy, one has therefore to have high angular resolution observations so as to distinguish between the *nuclear* component and the rest of the emission. With the present technology (angular resolution of a few seconds of arc) such a study would be possible only for extremely nearby galaxies. However, evidence for flattening of the “hard” (2–10 keV band) luminosity function at very low luminosities ($\leq 10^{42} \text{ ergs } s^{-1}$) is presented by Persic et al. (1989), who have studied it indirectly, using X-ray measurements of an optically selected sample of AGNs.

3.2. The Luminosity Function in Different Redshift Shells

The larger statistics available with respect to the MSS sample of AGNs (Maccararo et al. 1984) allows us, for the first time, to derive the AGN XLF at different redshifts directly from the data in a *model-independent* way. We have chosen to divide the sample into redshift slices in such a way that the slices correspond to a uniform increase in look-back time τ of 0.15. For $q_0 = 0$, τ is equal to $z/(1+z)$, and the corresponding redshifts ranges are 0.0–0.18; 0.18–0.43; 0.43–0.82; 0.82–1.50; and 1.50–3.0. The numbers of AGNs in each redshift shell are respectively 167, 137, 75, 56, and 13.

The individual luminosity functions do not overlap; rather, they show a systematic shift toward higher luminosities as one moves from low to high redshift. This is the expected signature of cosmological evolution for which Figure 6 shows *direct* evidence. It is worth noting that a “weak” evolution is evident at low redshifts ($z \leq 0.4$), while evolution becomes more evident for z larger than 0.4. We have previously noted that we sample different regions of the luminosity function at different redshifts. This is a consequence of dealing with a flux-limited sample. As a result we are not in a position to determine unequivocally from the data the evolutionary law which best describes the AGN behavior. To do so, a sampling of the luminosity function over a broader range of luminosities in each redshift shell is needed. Therefore, in the interest of brevity and simplicity we shall limit our analysis in the present work to the assumption of evolutionary models and the derivation of best-fit parameters. We expect, however, that the large statistics available and the current sampling of the luminosity redshift space will allow us to test, more stringently than was previously possible, whether the models assumed are an acceptable representation of the data.

4. THE COSMOLOGICAL EVOLUTION OF AGNs AND THEIR DE-EVOLVED X-RAY LUMINOSITY FUNCTION

A number of models have been proposed to describe the cosmological evolution of quasars. The major contending models have been the pure density evolution (PDE) model (Schmidt 1968) and the pure luminosity evolution (PLE) model (Mathez 1976, 1978). In the framework of the PDE model the

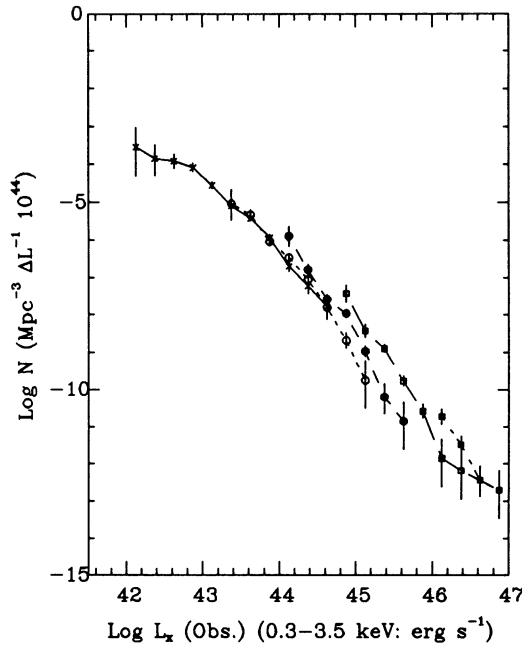


FIG. 6.—Luminosity functions derived in various redshift shells using the $1/V_a$ method (see § 3.2). The redshift ranges are 0.0–0.1765 (*crosses*), 0.1765–0.4286 (*open circles*), 0.4286–0.8182 (*filled circles*), 0.8182–1.50 (*open squares*) and 1.50–3.0 (*filled squares*). In each redshift slice data have been binned in bins of equal logarithmic width of 0.25; 1σ error bars are determined by the number of objects which contribute to each bin. Note that in the $z = 0.8182$ –1.50 luminosity function (*open squares*) there is one empty bin at $\langle L_x \rangle = 46.625$.

luminosity function is shifted, from early epochs to the present, along the density axis, preserving its shape. The luminosity of the objects does not change; it is their number which changes with cosmic time. PLE models instead conserve the number of objects as a function of cosmic time; it is their luminosity which changes. If the change in luminosity affects all objects equally, then the shape of the luminosity function is again conserved and the net result is a shift along the luminosity axis. More complicated models have been proposed, such as luminosity-dependent density evolution (Schmidt & Green 1983, 1986) and luminosity-dependent luminosity evolution (Cavaliere et al. 1983). In these latter cases the luminosity function also changes its shape. It has been shown that, in the case of quasars, PDE models fail to describe the observed counts at faint magnitudes. PDE models have thus lost their appeal, and we will not consider them in our analysis.

Here we will consider only PLE models with the two most commonly used evolutionary forms.

4.1. The Cosmological Evolution

A powerful tool for studying the cosmological evolution of a class of objects is the V/V_{\max} variable, first introduced by Schmidt (1968) for the case of a single sample, and adapted (V_e/V_a) to the more general case of the combination of several complete samples by Avni & Bahcall (1980). If the test is applied to a sample that is known to be complete, one can test whether the objects are uniformly distributed in the universe or not. In the case of a statistically complete sample of objects which are uniformly distributed, the above test yields a mean $\langle V_e/V_a \rangle = 0.50$ [$\text{rms} = (12N)^{-1/2}$, where N is the number of

objects in the sample] and a uniform distribution of the individual values of V_e/V_a between 0 and 1.

For our sample of objects we find that the hypothesis of a uniform distribution is rejected at more than the 99.99% confidence level ($\langle V_e/V_a \rangle = 0.6194 \pm 0.0136$). Thus we assume an evolution law and search for the value of the parameter which gives $\langle V_e/V_a \rangle = 0.5$ and the individual V_e/V_a values uniformly distributed between 0 and 1.

We discuss here only the case of pure luminosity evolution, and we consider the two most common evolutionary forms:

$$L_x(z) = L_x(0)e^{Cz} \quad (1)$$

and

$$L_x(z) = L_x(0)(1+z)^C, \quad (2)$$

where $L_x(0)$ is the present-epoch luminosity, C is the evolution parameter, and τ is the look-back time.

From our evolution analysis we find that, for the evolutionary law of equation (1), (a) the best-fit value for C is 4.18, and the associated 68% and 95% confidence intervals are 3.83–4.50 and 3.47–4.80, respectively, and (b) the pure luminosity evolution model considered is acceptable by the Kolmogorov-Smirnov (K-S) test at the 95% confidence level. In the case of the evolutionary law of equation (2), we find that (a) the best-fit value for C is 2.56, and the associated 68% and 95% confidence intervals are 2.39–2.73 and 2.19–2.88, respectively, and (b) the pure luminosity evolution model considered is acceptable by the K-S test at the 95% confidence level.

We note however, that the analysis of the luminosity function in different redshift shells (see Fig. 6) seems to indicate that the two simple PLE models tested are not an excellent representation of the data. There is no significant difference, in fact, between the first two luminosity functions, as if evolution begins only at redshifts greater than 0.4. This is an indication that the sample size is now large enough to require more complicated models. Use of the two adopted models is, however, justified by the interest in comparing the evolutionary behavior of X-ray-selected AGNs with previous results (Maccacaro et al. 1984) and with the behavior of optically selected and radio-selected quasars.

With respect to the previous analysis of X-ray-selected AGNs, we obtain here a best-fit value for the evolution parameter C of 4.18 ($\pm 1\sigma = 3.83$ –4.50), slightly lower than the value $C = 4.85$ found by Maccacaro et al. (1984) from the analysis of the MSS sample. If we consider that the estimate of Maccacaro et al. (1984) was affected by larger uncertainties because of the limited statistics available (the $\pm 1\sigma$ interval on C was 4.02–5.54), then the difference with the present result is fully within the statistical uncertainties.

The cosmological evolution and the luminosity function of optically selected quasars have been determined by several authors (see among others Schmidt & Green 1983) and more recently by Boyle et al. (1990), who have analyzed a sample of about 600 objects, comparable in size to the sample used in this work. These authors, in order to avoid possible incompleteness in their sample either at faint magnitudes or at low redshifts, have restricted their analysis to those objects with $M_B < -23$ and $z > 0.3$. Within the framework of the two luminosity evolution laws considered in this paper, they found a best-fit value of 7.0 (if the evolutionary law is e^{Cz}) and 3.46 [if the evolutionary law is $(1+z)^C$]. We can thus confirm that the X-ray evolution of quasars is slower than in the optical and radio domain, as first noted by Maccacaro & Gioia (1983). We emphasize,

however, that the X-ray-selected samples used contain both high-luminosity objects (quasars) and low-luminosity objects (Seyfert galaxies) and are dominated by low-redshift objects, while samples of optically selected quasars usually do not contain low-luminosity objects and are incomplete at a redshift less than 0.3.

More complicated models, including luminosity-dependent evolutionary models, will be considered in a separate paper, together with a study of a possible dependence of the evolutionary properties on other intrinsic AGN properties.

4.2. The Effect of Incompleteness on the Cosmological Evolution Analysis

In order to evaluate how the results derived are affected by the uncertainties on the actual number of AGNs in the remaining 31 unidentified sources, we have considered two extreme cases. In the first (S1, maximum incompleteness) we have considered only the 427 spectroscopically identified AGNs, as if no more AGNs were to be found among the unidentified sources. In the second case (S2) we have limited the analysis to that portion of the survey defined by $S_{\text{lim}} = 2.62 \times 10^{-13}$ ergs $\text{cm}^{-2} \text{s}^{-1}$. In this way, at the price of losing a considerable number of sources (see Table 2), we can deal with a virtually fully identified survey (incompleteness $< 1\%$) from which to extract the AGN sample.

The results obtained from the evolution analysis of samples S1 and S2 are shown in Figures 7a (evolutionary model of eq. [1]) and 7b (evolutionary model of eq. [2]), where the resulting values of $\langle V_e/V_a \rangle$ are plotted against the evolution parameter C . For comparison the result obtained using the original sample is also indicated. The two dotted lines indicate the 95% confidence region for C . As expected, the best-fit value for C for sample S1 is lower than that for sample S2. This reflects the incompleteness which affects S1 with respect to S2. At the same time, it is reassuring to notice that the best-fit values obtained

for S1 and S2 are very similar to each other and are consistent, given the statistical uncertainties, with the best-fit value obtained for our working sample.

We have then evaluated how the estimate of the cosmological evolution is affected by the uncertainties due to the redshifts assigned to the "expected" AGNs. We have thus assigned to the AGNs extreme redshift values in the following manner. We have assigned to each object (using the procedure explained in § 2) a redshift value such that the "real" value for z has a probability less than 10% of being lower than the assigned value (case $S_{z_{\text{low}}}$) or higher than the assigned value (case $S_{z_{\text{high}}}$). The results of the evolution analysis for these extreme cases are shown in Figures 8a (evolutionary model of eq. [1]) and 8b (evolutionary model of eq. [2]), where the value of $\langle V_e/V_a \rangle$ is reported as a function of the evolution parameter C for the original sample (solid line) and for the cases $S_{z_{\text{low}}}$ and $S_{z_{\text{high}}}$ (dashed lines). The influence of the actual value of the redshift assigned to the 21 "expected" AGNs on the best-fit evolution parameter C is negligible.

Thus we are confident that when the EMSS is fully identified, the results derived here on the AGN cosmological evolution will not change significantly.

4.3. De-evolved X-Ray Luminosity Function

As already discussed in § 4, in the framework of pure luminosity evolution, the luminosity function maintains the same shape, and the number of objects is conserved. The luminosity coordinate is simply shifted as a function of redshift, according to the chosen evolutionary law. The luminosity function we derived here is computed at $z = 0$; i.e., for each object we determine and use the zero-redshift luminosity, using for the evolution parameter C the best estimate obtained from the $\langle V_e/V_a \rangle$ test. This procedure has the advantage of allowing the use of the full sample of objects to study the luminosity function (at a given redshift) over the maximum possible range of

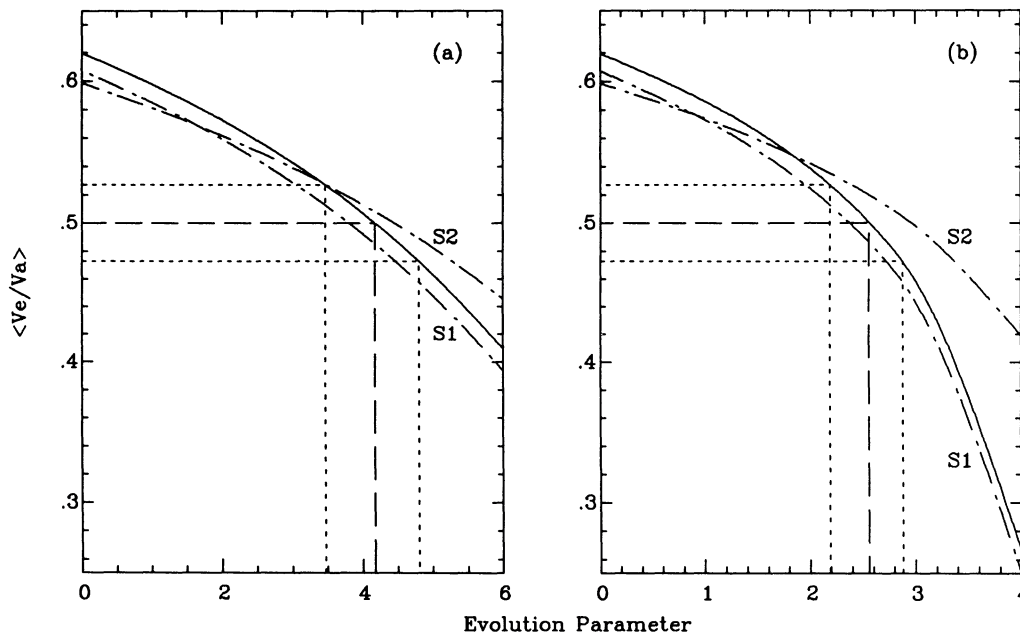


FIG. 7.—(a) Value of $\langle V_e/V_a \rangle$ as a function of the evolution parameter C for the original sample (solid line), sample S1, and sample S2 (see § 4.2) for the evolutionary law $L_x(z) = L_x(0)e^{Cz}$. (b) Value of $\langle V_e/V_a \rangle$ as a function of the evolution parameter C for the original sample (solid line), sample S1, and sample S2 (see § 4.2) for the evolutionary law $L_x(z) = L_x(0)(1+z)^C$. The two dotted lines indicate the 95% confidence region for C , while the dashed line indicates the best-fit value.

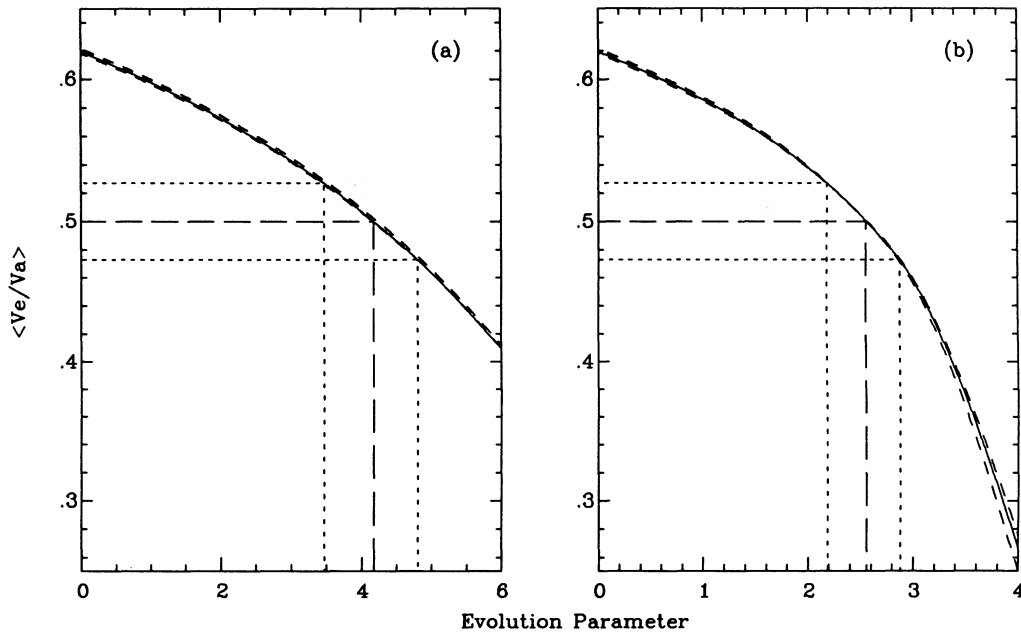


FIG. 8.—(a) Value of $\langle V_e/V_a \rangle$ as a function of the evolution parameter C for the original sample (solid line) and for the case $S_{z_{low}}$ and $S_{z_{high}}$ (short-dashed lines) (see § 4.2) for the evolutionary law $L_x(z) = L_x(0)e^{Cz}$. (b) Value of $\langle V_e/V_a \rangle$ as a function of the evolution parameter C for the original sample (solid line) and for the case $S_{z_{low}}$ and $S_{z_{high}}$ (short-dashed lines) (see § 4.2) for the evolutionary law $L_x(z) = L_x(0)(1+z)^C$. The two dotted lines indicate the 95% confidence region for C , while the dashed line indicates the best-fit value.

luminosities. Obviously, since the various objects are “moved” to the reference redshift from the redshift at which they are observed, one has to use the adopted evolutionary model, and best-fit parameter(s). Consequently, the luminosity function so derived is model-dependent. In general, steeper evolutionary laws and higher values of C lead to steeper luminosity functions (see Table 4).

Figure 9 shows the differential XLF obtained using the $1/V_a$ method. It has been computed at $z = 0$ using the PLE model of equation (1) with $C = 4.18$ (best fit). Data have been binned in bins of equal logarithmic width of 0.25. The 1σ error bars associated with the individual points are determined by the number of objects which contribute to that point. Errors have been computed using Poisson statistics. Figure 9 clearly indicates that a single power law is not an appropriate representation of the data over the whole range of luminosities sampled. The two power laws, shown in Figure 9, represent the best fit to the unbinned data using the maximum-likelihood method (see Murdoch, Crawford, & Jauncey, 1973 and references therein). At low luminosities [$L_x(0) < 2.5 \times 10^{43}$ ergs s^{-1}] the best-fit slope is $\gamma_1 = 1.35$, while at high luminosities the best-fit slope is $\gamma_2 = 3.05$. In Table 4 we report the variation of the XLF parameters as a function of the evolution parameter C . For each value of the evolution parameter C considered (best-fit

value and $\pm 95\%$ confidence interval) the fits have been computed between 3.16×10^{41} and 2.5×10^{43} ergs s^{-1} and between 2.5×10^{43} and infinite luminosity. The normalization coefficients K_1 and K_2 (in units of $\text{Mpc}^{-3} L_{44}^{\gamma-1}$) have been obtained by requiring that the number of expected objects equal the number of observed objects.

If the PLE model of equation (2) is used, the resulting de-evolved XLF is not significantly different. It can still be described by a broken power law, with best-fit slopes of 1.40 and 3.16 and a break luminosity of 3.6×10^{43} .

In Figure 10 we present the histogram of the de-evolved X-ray luminosity for the 427 spectroscopically classified AGNs and for the 21 “expected” AGNs (shaded area) obtained according to the evolutionary law of equation (1). The bins are identical to those used in Figure 9.

The AGN XLF shown in Figure 9 (de-evolved at $z = 0$) and in Figure 6 (observed) cover the range of X-ray luminosities from 1.4×10^{42} to 7.4×10^{45} ergs s^{-1} and from 1.6×10^{42} to 8.5×10^{46} ergs s^{-1} , respectively. Objects with luminosity outside this range are not observed. We can check whether this is evidence of a further change in the XLF slope [more pronounced flattening at $L_x(0) < 10^{42}$ ergs s^{-1} and/or steepening at $L_x(0) > 10^{46}$ ergs s^{-1}] or whether it simply reflects the limitations of the EMSS survey (in terms of sensitivity and/or

TABLE 4
VARIATION OF XLF PARAMETERS WITH EVOLUTION PARAMETER C
[Evolutionary Model $L_x(z) = L_x(0)e^{Cz}$]

C	γ_1, K_1 ($\text{Mpc}^{-3} L_{44}^{\gamma-1}$) [$L_x(0) < 2.5 \times 10^{43}$ ergs s^{-1}]	γ_2, K_2 ($\text{Mpc}^{-3} L_{44}^{\gamma-1}$) [$L_x(0) > 2.5 \times 10^{43}$ ergs s^{-1}]
3.47 (-2σ)	1.32, 1.7×10^{-6}	2.89, 2.0×10^{-7}
4.18 (best fit)	1.35 ± 0.13 , 1.5×10^{-6}	3.05 ± 0.05 , 1.4×10^{-7}
4.80 ($+2\sigma$)	1.42, 1.1×10^{-6}	3.22, 9.7×10^{-8}

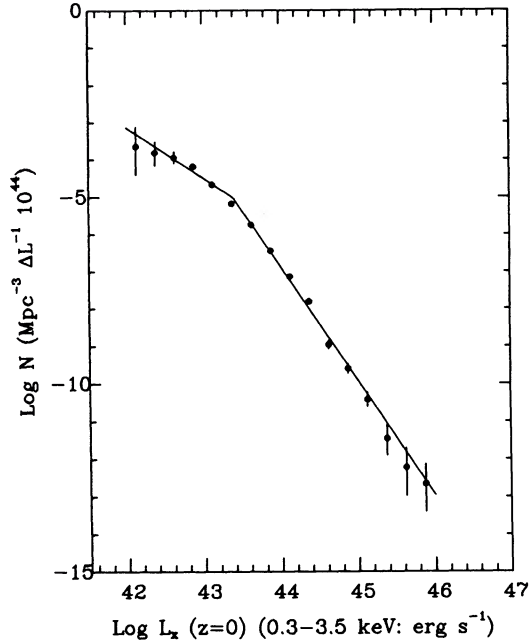


FIG. 9.—Differential X-ray luminosity function, computed at $z = 0$ according to the evolutionary law $L_x(z) = L_x(0)e^{cz}$ (see § 4.3). Data have been binned in bins of equal logarithmic width of 0.25; 1σ error bars are determined by the number of objects which contribute to each bin. The two power laws represent the best fit to the *unbinned data* using the maximum-likelihood method. The high-luminosity [$L_x(0) > 2.5 \times 10^{43}$ ergs s^{-1}] best-fit slope is 3.05, while the low-luminosity best-fit slope is 1.35.

volume searched). We have estimated that, extrapolating the XLF at low luminosities with the same slope $\gamma_1 = 1.35$ which describes it at $L_x(0) < 2.5 \times 10^{43}$ ergs s^{-1} , only two sources are expected in the EMSS with luminosity in the interval 10^{41} – 10^{42} ergs s^{-1} . We see none. With a similar procedure we have estimated that, extrapolating the XLF at high luminosities

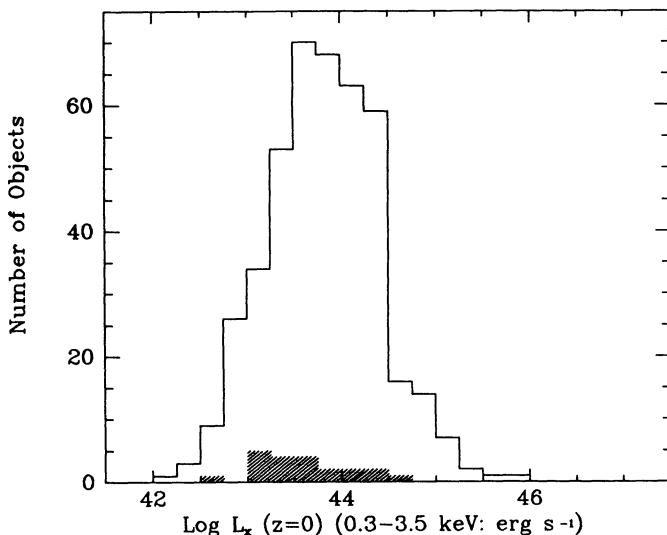


FIG. 10.—The 0.3–3.5 keV de-evolved ($z = 0$) X-ray luminosity distribution for the 427 spectroscopically classified AGNs and for the 21 “expected” AGNs (shaded areas). Luminosities have been computed at $z = 0$ according to the evolutionary law $L_x(z) = L_x(0)e^{cz}$ (see § 4.3). The bins are identical to those used in Fig. 3 and in Fig. 9.

with $\gamma_2 = 3.05$, only 0.8 objects are expected in the EMSS with luminosity in the interval 10^{46} – 10^{48} ergs s^{-1} . We see none. Similar results are obtained using the numerical values for γ_1 and γ_2 which best describe the luminosity function de-evolved according to the evolutionary model of equation (2). The absence of extremely high luminosity objects in the survey is then due to the limited volume surveyed given their low volume density. Therefore, we cannot comment on the shape of the XLF outside the range sampled, in the sense that we have no evidence for a slope change.

Having determined the X-ray luminosity function and cosmological evolution of AGNs, we can now make a direct estimate of their contribution, as a class, to the diffuse X-ray background radiation.

5. THE AGN CONTRIBUTION TO THE DIFFUSE EXTRAGALACTIC X-RAY BACKGROUND

Since its discovery (Giacconi et al. 1962), the origin of the diffuse X-ray background (XRB) has remained a subject of controversy (see, among others, Giacconi & Zamorani 1987, Boldt 1987, and Setti 1990 for recent reviews of the subject). Schwartz & Gursky (1974) showed that even with no evolutionary effects a significant fraction of the flux of the XRB should originate at a redshift greater than unity. This suggests that the study of the XRB might provide information on events occurring at an early epoch.

The most favored model to explain the origin of the diffuse XRB radiation is emission from discrete sources (Giacconi et al. 1962). This model has received considerable support by the analysis of the *Einstein* Deep Survey (Giacconi et al. 1979) and by the discovery that AGNs, as a class, are strong X-ray emitters (Tananbaum et al. 1979; Zamorani et al. 1981). More recently the results of the *Cosmic Background Explorer* (Mather et al. 1990) seem to have put to rest the suggestion that a significant fraction of the diffuse XRB radiation is due to truly diffuse emission from a hot intergalactic medium. Mather et al. (1990) have in fact inferred, from the measurement of the cosmic microwave background spectrum and its very small deviation from a blackbody shape, that diffuse X-ray emission accounts for less than 3% of the XRB intensity.

As discussed by Maccacaro et al. (1984), short of resolving the XRB with extremely deep, high-resolution X-ray images, the best way to determine the contribution to the XRB from a particular class of sources is to integrate its luminosity function (determined directly from the X-ray data), taking into account its evolution with cosmic time.

The spectrum of the XRB is well fitted by an isothermal bremsstrahlung model corresponding to an optically thin, hot plasma with kT of the order of 40 keV (Marshall et al. 1980); in the 3–100 keV energy band it may be approximated by (Boldt & Leiter 1984)

$$I_{\text{XRB}}(E) = A(E/3)^{-0.29} e^{-E/40}, \quad (3)$$

where E is the photon energy (in keV), $A = 5.6$ keV cm^{-2} s^{-1} sr^{-1} keV^{-1} , and $I_{\text{XRB}}(E)$ is the measured intensity of the XRB.

Since the large majority of the extragalactic X-ray sources have been measured in the soft X-ray energy band ($E < 4$ keV) (with the *Einstein Observatory* or *EXOSAT*), while the XRB is well known for energies greater than 3 keV, it is common practice to refer the AGN contribution to the XRB at an energy of 2 keV. To obtain the XRB intensity at 2 keV, we have made the assumption that equation (3) holds to this energy. We find $I_{\text{XRB}}(2 \text{ keV}) = 5.99$ keV cm^{-2} s^{-1} sr^{-1} keV^{-1} . If the XRB

spectrum turns up below 3 keV as indicated by Micela et al. (1990) and by Wu et al. (1990), then the estimate of the AGN contribution to the 2 keV XRB can be viewed as upper limit. Nevertheless, our determination of the total intensity produced by the AGNs is *independent* of the intensity of the XRB and therefore is not affected by the uncertainties which affect the estimate of the XRB.

Since we have derived a parametric representation of the XLF over the entire range of luminosities sampled, we compute the contribution of the AGNs to the XRB intensity by integration of the parametric representation of the XLF.

The intensity of the XRB at energy E_0 due to AGNs can be calculated, in the case of $q_0 = 0$, from the equation (Schwartz 1979)

$$I(E_0) = \frac{c}{4\pi H_0} \int_0^{+\infty} \frac{B[E_0(1+z); z]}{(1+z)^5} dz, \quad (4)$$

where $B[E_0(1+z); z]$ is the AGN volume emissivity at energy $E = E_0(1+z)$ and redshift z .

In the framework of the PLE model given in equation (1), and assuming an X-ray spectral index of 1 (derived in the spectral analysis to the extragalactic EMSS sources; Maccacaro et al. 1988), the AGN volume emissivity at energy $E = E_0(1+z)$ and at redshift z is given by

$$B[E; z] = B[E_0; z = 0](1+z)^2 e^{C\tau}, \quad (5)$$

where C and τ have been defined in § 4.1 and $B[E_0; z = 0]$ is the AGN local volume emissivity at energy E_0 .

If $dN_0(L)/dL$ is the differential XLF referred to $z = 0$, then

$$B[E_0; z = 0] = \int_{L(0)_{\min}}^{L(0)_{\max}} \frac{dN_0(L)}{dL} L dL \quad (6)$$

is the local volume emissivity derived from objects with luminosity between $L(0)_{\min}$ and $L(0)_{\max}$. In our case we have found, in § 4.3, that

$$\frac{dN_0(L_{44})}{dL_{44}} = \begin{cases} K_1 L_{44}^{-\gamma_1}, & L_x(0) < 2.5 \times 10^{43} \text{ ergs s}^{-1}, \\ K_2 L_{44}^{-\gamma_2}, & L_x(0) > 2.5 \times 10^{43} \text{ ergs s}^{-1}. \end{cases} \quad (7)$$

where K_1 , K_2 , γ_1 , and γ_2 are the differential XLF parameters reported in Table 4 and L_{44} is the luminosity expressed in units of 10^{44} ergs s^{-1} .

From equations (4), (5), (6), and (7) we can obtain

$$I(E_0) = 1.272 \times 10^6 E_0^{-1} \int_{L(0)_{44, \min}}^{L(0)_{44, \max}} \frac{dN_0(L_{44})}{dL_{44}} \times L_{44} dL \int_{z_{\min}}^{z_{\max}} (1+z)^{-3} e^{C\tau} dz. \quad (8)$$

Because of the shape of the XLF (steep at high luminosities and flat at low luminosities, the computation of the AGN intensity does not depend critically on the values of L_{\min} and L_{\max} . Moreover, within the framework of the evolutionary law of equation (1), we have estimated that only 6.2 sources are expected in the EMSS with redshift between 2 and 3. This number increases to 11.8 if the evolutionary law of equation (2) is used. We see 4 ($z = 2.027, 2.095, 2.410, \text{ and } 2.830$). These results allow us to integrate the XLF consistently over the *observed* range of luminosities and redshifts [between $L(0)_{\min} = 10^{41}$ and $L(0)_{\max} = 10^{47}$ ergs s^{-1} and between $z_{\min} = 0$ and $z_{\max} = 3.0$] to obtain an estimate of their intensity. We stress that this contribution comes from objects that we have

TABLE 5
CONTRIBUTION FROM AGNS TO THE 2 keV XRB

z_{\max}	-2σ	Best Fit	$+2\sigma$
3.0.....	32% (33%)	37% (40%)	45% (48%)
3.5.....	34% (36%)	40% (45%)	48% (55%)
4.0.....	35% (39%)	42% (50%)	51% (63%)

NOTE.—Numbers in parentheses refer to the evolutionary model of eq. (2).

actually *seen* and does not result from the extrapolation of the measured properties to a redshift or luminosity domain not sampled. We obtain a 2 keV AGN intensity of $2.23 \text{ keV cm}^{-2} \text{ s}^{-1} \text{ sr}^{-1} \text{ keV}^{-1}$. This corresponds to 37% of the keV XRB intensity.

This result is a weak function of the evolution parameter used and of the associated XLF. Using for C the values 3.47 and 4.80 (95% confidence interval for C) and the corresponding XLF (see Table 4), the fractions of 2 keV XRB intensity accounted for by the AGNs become 32% and 45%, respectively. We have also investigated how the results depend on the evolutionary model chosen and/or on the limit chosen for the integration over redshifts. The results are summarized in Table 5 (the values reported in parentheses represent the fraction of the 2 keV XRB intensity computed using the evolutionary law of eq. [2]).

Using equation (8), we have also computed the percentage contribution to the 2 keV AGN intensity from the different bins of luminosity and redshift. These results are reported in Table 6. It is worth noting that about 85% of the 2 keV AGN intensity comes from objects with $L_x(0)$ between 10^{42} and 10^{44} ergs s^{-1} . A third of the overall contribution is due to objects in the redshift range 1–2.

The present “best-fit” estimate of the AGN contribution to the diffuse XRB is significantly lower than the “best-fit” estimate of Maccacaro et al. (1984) (37% versus 79%). This is due mainly to two reasons. First, the best-fit value for the evolution parameter C is slightly lower than it was in Maccacaro et al. (1984). Using $C = 4.02$ (a value closer to the current best fit of 4.18) Maccacaro et al. (1984) in fact found a contribution of $53^{+30}_{-11}\%$ which compares better with the present estimate of 37%. Second, following the spectral analysis of Maccacaro et al. (1988) of the EMSS sources, we have used in the present work an energy spectrum with slope $\alpha = 1$ to characterize the AGN population. Therefore, the present estimate, being based

TABLE 6
PERCENTAGE CONTRIBUTION TO THE 2 keV AGN INTENSITY FROM THE DIFFERENT BINS OF LUMINOSITY AND REDSHIFT [Evolutionary Model $L_x(z) = L_x(0)e^{C\tau}$]

log $L_x(0)$ ($L_{\min} - L_{\max}$)	REDSHIFT RANGE				REDSHIFT RANGE 0.0–3.0
	0.0–0.5	0.5–1.0	1.0–2.0	2.0–3.0	
41–42.....	1.43	1.38	1.97	1.16	5.94
42–43.....	6.43	6.21	8.84	5.22	26.70
43–44.....	14.02	13.54	19.28	11.38	58.22
44–45.....	2.01	1.94	2.76	1.63	8.34
45–46.....	0.18	0.17	0.25	0.15	0.75
46–47.....	0.02	0.02	0.02	0.01	0.07
41–47.....	24.09	23.26	33.12	19.55	100

on much tighter determination of several critical parameters, represents a significant improvement over the previous estimate of the AGN contribution to the diffuse X-ray background and, within the unavoidable limitation of the current data set, is the best possible estimate.

6. SUMMARY AND CONCLUSIONS

The high identification rate (96%) presently available for the *Einstein* Extended Medium-Sensitivity Survey has allowed us to extract a sample of more than 420 X-ray-selected AGNs exclusively defined by their X-ray properties. Using the available information, we have also corrected for the effect of the present slight incompleteness of the sample. We have shown that the results presented here will not significantly change once the identification process is completed.

The number of objects in the AGN sample, and their coverage of the log z -log L_x plane, have permitted us to derive the local ($z < 0.1$) observed XLF as well as the XLF in different redshift shells up to $z \sim 2$. The local XLF shows a substantial flattening for $L_x \leq 5 \times 10^{42}$ ergs s^{-1} . We have compared our local XLF with the *HEAO 1 A-2* local XLF (converted into the 0.3–3.5 keV energy band). For luminosities greater than $\sim 2 \times 10^{43}$ ergs s^{-1} a good agreement is shown between the two local XLFs, which are both well described by a single power law. At lower luminosities the XLF obtained from the EMSS AGN sample is flatter than the one obtained from the “harder” *HEAO 1 A-2* sample. Intrinsic absorption in low-luminosity objects could be responsible for this difference.

The AGN XLFs at different redshifts have been obtained in a model-independent way. These XLFs give *direct* evidence for cosmological evolution. Weak evolution is evident for $z < 0.4$, while the evolution becomes more pronounced for z larger than 0.4.

In order to compare the results of our evolution analysis with those discussed in the literature, the data have been analyzed within the framework of pure luminosity evolution

models. We have considered the two most common evolutionary forms:

$$L_x(z) = L_x(0)e^{Ct} \quad \text{and} \quad L_x(z) = L_x(0)(1+z)^C.$$

Best-fit values of 4.18 and 2.56, respectively, have been obtained for the evolution parameters of the two chosen evolutionary laws. This result confirms and strengthens the evidence for “slower” evolution of X-ray-selected AGNs relative to optically selected QSOs.

Using the full sample of objects, and within the framework of the assumed evolutionary laws, we have derived the de-evolved X-ray luminosity function. A good fit with a broken power law has been obtained. The high-luminosity [$L_x(0) > 2.5 \times 10^{43}$ ergs s^{-1}] best-fit slope is 3.05, while the low-luminosity best-fit slope is 1.35. We have no evidence for a further slope change outside the range of luminosities sampled.

Having a determination of the XLF and its evolution, we have estimated the contribution from AGNs to the diffuse X-ray background. Such an estimate, based upon the X-ray luminosity function and its evolution, is more reliable than estimates based upon an optical luminosity function plus an L_x - L_0 relation. We find a value of about 40% for their contribution to the 2 keV XRB. About 85% of this contribution comes from objects with $L_x(0)$ between 10^{42} and 10^{44} ergs s^{-1} .

We would like to thank G. Zamorani and G. G. C. Palumbo for useful discussions. Part of the data analysis has been done using the Distributed Information Retrieval from Astronomical Files (DIRA) developed by the Astronet Working Group on Database and Documentation. This work has received partial financial support from NASA contract NAS 8-30751, NASA grants NAG8-738 and NAG5-1256, NSF grant AST 87-15983, and the Smithsonian Institution Scholarly Studies grant SS88-3-87.

REFERENCES

- Avni, Y., & Bahcall, J. N. 1980, *ApJ*, 235, 694
 Boldt, E. 1987, *Phys. Rept.*, 146, 215
 Boldt, E. A., & Leiter, D. 1984, *ApJ*, 276, 427
 Boyle, B. J., Fong, R., Shanks, T., & Peterson, B. A. 1990, *MNRAS*, 243, 1
 Cavaliere, A., Giallongo, E., Messina, A., & Vagnetti, F. 1983, *ApJ*, 269, 57
 Cleary, M. N., Heiles, C., & Haslam, C. G. T. 1979, *A&AS*, 36, 95
 Danese, L., DeZotti, G., Fasano, G., & Franceschini, A. 1986, *A&A*, 161, 1
 Della Ceca, R., Palumbo, G. G. C., Persic, M., Boldt, E. A., De Zotti, G., & Marshall, E. E. 1990, *ApJS*, 72, 471
 Fabbiano, G. 1989, *ARA&A*, 27, 87
 Giacconi, R., et al. 1979, *ApJ*, 234, L1
 Giacconi, R., Gursky, J., Paolini, F., & Rossi, B. 1962, *Phys. Rev. Letters*, 9, 439
 Giacconi, R., & Zamorani, G. 1987, *ApJ*, 312, 503
 Gioia, I. M., Maccacaro, T., Schild, R. E., Wolter, A., Stocke, J. T., Morris, S. L., & Henry, J. P. 1990, *ApJS*, 72, 567
 Heiles, C., & Cleary, M. N. 1979, *Australian J. Phys. Ap. Suppl.*, 46, 1
 Maccacaro, T., & Gioia, I. M. 1983, in *Early Evolution of the Universe and Its Present Structure*, ed. G. O. Abell & G. Chincarini (Dordrecht: Reidel), 7
 Maccacaro, T., Gioia, I. M., & Stocke, J. T. 1984, *ApJ*, 283, 486
 Maccacaro, T., Gioia, I. M., Wolter, A., Zamorani, G., & Stocke, J. T. 1988, *ApJ*, 326, 680
 Maccacaro, T., et al. 1991, in preparation
 Marshall, F. E., Boldt, E. A., Holt, S. S., Miller, R. B., Mushotzky, R. F., Rose, L. A., Rothschild, R. E., & Serlemitsos, P. J. 1980, *ApJ*, 235, 4
 Mather, J. C., et al. 1990, *ApJ*, 354, L37
 Mathez, G. 1976, *A&A*, 53, 15
 ———. 1978, *A&A*, 68, 71
 Micela, G., Harnden, F. R., Rosner, R., Sciortino, S., & Vaiana, G. S. 1990, in *Proc. 23d ESLAB Symposium (Bologna), X-Ray Astronomy*, ed. J. Hunt & B. Batrick (Paris: ESA), 1005
 Murdoch, H. S., Crawford, D. E., & Jauncey, D. L. 1973, *ApJ*, 183, 1
 Persic, M., De Zotti, G., Danese, L., Palumbo, G. G. C., Franceschini, A., Boldt, E. A., & Marshall, F. E. 1989, *ApJ*, 344, 125
 Piccinotti, G., Mushotzky, R. F., Boldt, E. A., Holt, S. S., Marshall, F. E., Serlemitsos, P. J., & Shafer, R. A. 1982, *ApJ*, 253, 485
 Schmidt, M. 1968, *ApJ*, 151, 393
 Schmidt, M., & Green, R. F. 1983, *ApJ*, 269, 352
 ———. 1986, *ApJ*, 305, 68
 Schwartz, D. A. 1979, in *Proc. Symposium of the 21st Plenary Meeting of COSPAR (Innsbruck), X-Ray Astronomy*, ed. W. A. Baity & L. E. Peterson (Oxford and New York: Pergamon), 453
 Schwartz, D., & Gursky, H. 1974, in *X-Ray Astronomy*, ed. R. Giacconi & H. Gursky (Dordrecht: Reidel), 359
 Setti, G. 1990, in *IAU Symposium 139, Galactic and Extragalactic Background Radiation*, ed. S. Bowyer & Ch. Leinert (Dordrecht: Kluwer), 345
 Stark, A. A., Heiles, C., Bally, J., & Linker, R. 1989, private communication
 Stocke, J. T., Morris, S. L., Gioia, I. M., Maccacaro, T., Schild, R., Wolter, A., & Henry, J. P. 1991, *ApJS*, in press
 Tananbaum, H., et al. 1979, *ApJ*, 234, L9
 Warwick, R. S., & Stewart, G. C. in *Proc. 23d ESLAB Symposium (Bologna), X-Ray Astronomy*, ed. J. Hunt & B. Batrick (Paris: ESA), 727
 Wu, X., Hamilton, T., Helfand, D., & Wang, Q. 1990, *CAL Preprint No. 400*.
 Zamorani, G., et al. 1981, *ApJ*, 245, 357